



Two-dimensional affine model-based estimators for principal strain vascular ultrasound elastography with compound plane wave and transverse oscillation beamforming

Hongliang Li^{a,b}, Jonathan Porée^{a,b}, Marie-Hélène Roy Cardinal^a, Guy Cloutier^{a,b,c,*}

^a Laboratory of Biorheology and Medical Ultrasonics, University of Montreal Hospital Research Center (CRCHUM), Montréal, QC, Canada

^b Institute of Biomedical Engineering, University of Montreal, Montréal, QC, Canada

^c Department of Radiology, Radio-Oncology and Nuclear Medicine, University of Montreal, Montréal, QC, Canada

ARTICLE INFO

Keywords:

Ultrasound elastography
Compound plane wave imaging beamforming
Transverse oscillation beamforming
Optical flow estimation
Phase estimation
Affine model-based estimation
Tissue incompressibility

ABSTRACT

Polar strain (radial and circumferential) estimations can suffer from artifacts because the center of a non-symmetrical carotid atherosclerotic artery, defining the coordinate system in cross-sectional view, can be mis-registered. Principal strains are able to remove coordinate dependency to visualize vascular strain components (i.e., axial and lateral strains and shears). This paper presents two affine model-based estimators, the affine phase-based estimator (APBE) developed in the framework of transverse oscillation (TO) beamforming, and the Lagrangian speckle model estimator (LSME). These estimators solve simultaneously the translation (axial and lateral displacements) and deformation (axial and lateral strains and shears) components that were then used to compute principal strains. To improve performance, the implemented APBE was also tested by introducing a time-ensemble estimation approach. Both APBE and LSME were tested with and without the plane strain incompressibility assumption. These algorithms were evaluated on coherent plane wave compounded (CPWC) images considering TO. LSME without TO but implemented with the time-ensemble and incompressibility constraint (Porée et al., 2015) served as benchmark comparisons. The APBE provided better principal strain estimations with the time-ensemble and incompressibility constraint, for both simulations and *in vitro* experiments. With a few exceptions, TO did not improve principal strain estimates for the LSME. With simulations, the smallest errors compared with ground true measures were obtained with the LSME considering time-ensemble and the incompressibility constraint. This latter estimator also provided the highest elastogram signal-to-noise ratios (SNRs) for *in vitro* experiments on a homogeneous vascular phantom without any inclusion, for applied strains varying from 0.07% to 4.5%. It also allowed the highest contrast-to-noise ratios (CNRs) for a heterogeneous vascular phantom with a soft inclusion, at applied strains from 0.07% to 3.6%. In summary, the LSME outperformed the implemented APBE, and the incompressibility constraint improved performances of both estimators.

1. Introduction

In recent years, noninvasive vascular elastography (NIVE) has gained increasing attention for evaluating the functionality of superficial arteries. Principal strains are able to remove coordinate dependency to visualize vascular strain components [1]. Currently, most two-dimensional (2-D) elastography algorithms are based on the cross-correlation, either in the space domain [2–10] or frequency domain [11–13], or based on registration methods [14,15]. With known axial (along the ultrasound beam) and lateral (perpendicular to it)

displacements between pre- and post-motion image blocks, axial and lateral strains and shears were computed from estimated displacement derivatives in respective directions [5,7,11,12]. Since associated high frequency displacement noise enhances the variance of such strain estimators, the least squares strain estimator (LSQSE) was proposed to increase the signal-to-noise ratio (SNR) by a piecewise linear fit [2,4,8,10]. However, tissue motion in the imaging plane may be complex and does not necessarily only undergo rigid transformations (translations and rotations), but also compression and expansion [16]. The signal distortion caused by such complex deformations induces

* Corresponding author at: Laboratory of Biorheology and Medical Ultrasonics, University of Montreal Hospital Research Center (CRCHUM), Montréal, QC, Canada.

E-mail address: guy.cloutier@umontreal.ca (G. Cloutier).

<https://doi.org/10.1016/j.ultras.2018.07.012>

Received 12 December 2017; Received in revised form 26 April 2018; Accepted 20 July 2018

Available online 21 July 2018

0041-624X/ © 2018 Elsevier B.V. All rights reserved.

decorrelation effects. Signal processing strategies, such as temporal stretching [17] and iterative coarse-to-fine approaches [4,18,19], have been used to reduce decorrelation noise. Other estimators were also proposed to reduce decorrelation noise by considering axial strain or axial shear [14,20,21].

In addition to abovementioned rigid model-based estimators, an alternative strategy is the affine model-based estimation methodology, which considers all non-rigid deformations of the tissue. Space-domain and phase-domain affine model-based methods have been investigated for cross-sectional imaging of arteries [22–25] and cardiac structures [26]. One of them is a registration-based algorithm [23]. It minimized a cost function using a numerical optimization method and improvements in SNR and contrast-to-noise ratio (CNR) were reported on axial strain estimations compared to the 2-D cross-correlation, but at a higher computational time cost.

Two other space-domain methods based on optical flow (OF) were proposed. In [25], a two-step OF strategy was reported to improve the performance of the axial strain estimation. More specifically, the OF estimation was performed sequentially two times and the two axial strain estimates were recombined. However, shear components were unable to be recombined and the lateral strain was also not considered. Furthermore, this latter approach [25] requires extra computational load due to an additional OF estimation. The other affine method is the OF-based Lagrangian speckle model estimator (LSME). In [24], Mercure et al. concluded that this approach performed better than an optimization-based LSME due to its reliability and computational efficiency. In [27], an OF-based LSME involving a constrained motion model was developed to provide robust 2-D principal strain estimations. Another method with an affine model is the affine phase-based estimator (APBE) [26], inspired by the phase-based estimator (PBE) [28–30]. This algorithm demonstrated a more accurate lateral estimation for cardiac motions than the standard block matching algorithm.

To perform cross-sectional scans in the context of NIVE, lateral estimations are particularly challenging due to the lower lateral than axial resolution of conventional focusing imaging, and the lack of phase information in the lateral direction. To overcome this limitation, several methods have been introduced. One assumes tissue incompressibility to improve the quality of lateral displacements [31], and SNR and CNR of elastograms [11,27]. Konofagou and Ophir used the lateral weighted interpolation of radiofrequency (RF) data to improve lateral displacement estimations [32]. However, the lateral interpolation and iterative scheme increase computational complexity [33].

Angular compounding schemes were also proposed to obtain lateral strain with more accurate axial estimations at multiple beam steering angles, using conventional focusing imaging [8,34–36]. Another way is to use advanced beamforming methods to enable more accurate lateral estimations. Korukonda and Doyley [5,37] demonstrated that synthetic aperture imaging could improve lateral NIVE estimates because of the high lateral sampling frequency and narrow lateral beamwidth. However, due to the single element emission, the low transmit power might

be insufficient for the clinical use of NIVE [38]. Hansen et al. reported that elastograms obtained with plane-wave angular compounding were comparable to standard focusing angular compounding [39]. Plane wave images are known, however, to exhibit low contrast and low resolution due to the lack of transmit focusing [40].

Alternatively, coherent plane wave compounding (CPWC) beamforming was proposed to solve these issues [41]. Under the framework of CPWC imaging, superior lateral strains and shears were obtained, compared with conventional OF-based LSME using standard focusing, by considering the incompressibility constraint and a time-ensemble approach [27]. Transverse oscillation (TO) beamforming [42,43] was also proposed to improve lateral estimations for vector velocity [44], cardiac motion [26] and longitudinal vascular wall motion [45] assessments. In [46], TO was adapted to plane wave imaging using a Fourier domain beamforming. In the context of cross-sectional NIVE, however, the OF-based LSME and APBE using the combined CPWC and TO imaging beamforming (CPWC&TO) have not yet been studied.

In this manuscript, we provide a performance evaluation of different elastography estimators and image beamforming schemes for cross-sectional carotid artery scanning. Validations were performed with simulations and *in vitro* phantom experiments. Overall, three contributions were made in this paper. One contribution is on the performance evaluation of two affine model-based estimators in the same framework of high-frame-rate imaging. Those estimators are determining simultaneously, using a minimization process, the translation (axial and lateral displacements) and deformation (axial and lateral strains and shears) components that were then used to compute principal strains. The second contribution is on the development of the affine-based APBE, and the introduction of a time-ensemble approach and an incompressibility constraint, as proposed in [27] for the OF-based LSME. Those improvements provided better principal strain estimations than previous APBE. The third contribution is the introduction of transverse oscillations (TO) into the LSME and the verification that TO imaging may be helpful for principal strain estimations when the tissue structure is complex and heterogeneous. In this study, the OF-based LSME of [27] is used as a benchmark comparison method. A list of abbreviations used in this paper is given in Table 1.

2. Theory

2.1. Image formation

2.1.1. Coherent plane wave compounding beamforming

Ultrafast plane wave imaging only needs a simultaneous single pulse emission on all selected transducer elements to produce a plane wave illumination unlike the conventional line-by-line scanning mode. The image generated by this scheme, however, has low image resolution and contrast due to the lack of transmit focusing [40]. Montaldo et al. [41] proposed a coherent plane wave compounding beamforming to enhance the image quality without sacrificing significantly the high frame rate capability. Each point of an image formed by one single

Table 1
List of abbreviations.

CPWC	Coherent Plane Wave Compounding beamforming
TO	Transverse Oscillation beamforming
CPWC&TO	Coherent Plane Wave Compounding with Transverse Oscillation beamforming
APBE	Affine Phase-Based Estimator
LSME	Lagrangian Speckle Model Estimator
CPWC&TO + APBE	APBE tested on CPWC&TO data
CPWC&TO* + APBE	APBE tested on CPWC&TO data with heterodyne demodulation
CPWC&TO + APBE ^T	APBE with the time-ensemble approach tested on CPWC&TO data
CPWC&TO + APBE ^{T&I}	APBE with the time-ensemble approach and the incompressibility constraint tested on CPWC&TO data
CPWC&TO + LSME ^T	LSME with the time-ensemble approach tested on CPWC&TO data
CPWC&TO + LSME ^{T&I}	LSME with the time-ensemble approach and the incompressibility constraint tested on CPWC&TO data
CPWC + LSME ^{T&I}	LSME with the time-ensemble approach and the incompressibility constraint tested on CPWC data (benchmark reference of [27])

plane wave is obtained by summing RF signals along transducer elements using certain delays, as given by [41]:

$$s(x, z) = \int RF(x_i, \tau_{TX} + \tau_{RX}) dx_i, \quad (1)$$

where the coordinate x, z corresponds to the image plane, x_i is the position of the receiving transducer element, $\tau_{TX} = (z \cos \theta + x \sin \theta)/c$, $\tau_{RX} = \sqrt{z^2 + (x - x_i)^2}/c$, where τ_{TX} and τ_{RX} are the emission and receive delays, respectively, θ is the angle of the emission pulse, and c is the speed of sound. Once the image for one single plane wave is beamformed, the compounded image is obtained by summing coherently all beamformed images with several plane waves at different angles. Twenty-one emissions between -10° and 10° with a 1° increment provided the best image quality for vascular strain imaging using the ultrasound probe of the current study [27]. Therefore, we kept this configuration for simulations and *in vitro* experiments.

2.1.2. Filtering-based TO beamforming using CPWC images

Transverse oscillation beamforming allows producing lateral phase information in ultrasound images. Classical TO imaging requires a specific apodization function in reception, made of two Gaussian peaks, to modulate the frequency spectrum of the beamformed TO image into four identified spots [45,47]. The following equation describes this apodization function w_i :

$$w_i = \frac{1}{2} \left(e^{-\pi \left(\frac{x_i - x_0}{\sigma_x} \right)^2} + e^{-\pi \left(\frac{x_i + x_0}{\sigma_x} \right)^2} \right), \quad (2)$$

where x_i is the position of the transducer element, $x_0 = \lambda_z z / \lambda_x$, $\sigma_x = \sqrt{2} \lambda_z z / \sigma_x$, λ_z is the transmitted pulse wavelength, z is the depth of interest, λ_x is the expected lateral oscillation wavelength, and σ_x is the full width at half maximum (FWHM) of the Gaussian envelope. It can be noticed in (2) that the apodization function must be changed dynamically as a function of depth z to keep a constant lateral oscillation wavelength during image beamforming. In addition, to implement different TO parameters (*i.e.*, λ_x and σ_x) one needs to beamform the raw data again.

To overcome these limitations and allow determining proper parameters, a filtering (or convolution) method was used to generate TO images [45]. In theory, TO filtering is able to generate oscillations with any lateral wavelengths. One advantage of the TO filtering method is that it is easy to control and obtain optimal TO parameters. Such post-processing approach only needs to filter beamformed data using different TO parameters and does not require access to pre-beamformed data using different apodization functions. The filtering or convolution is only performed along the lateral direction if RF images are used, while both lateral and axial directions should be filtered when B-mode images are considered. In this paper, we choose to filter each line of a RF CPWC image by multiplying it with two modulated Gaussian functions in the Fourier domain, as given by (3). The filtered frequency pattern of a RF image was made of four spots with an expected lateral oscillation frequency. This filter Ω is available in the public domain [48] as a Matlab graphical user interface. It is given by:

$$\Omega = e^{-2 \left(\pi \sigma_x \left(x_f - \frac{1}{\lambda_x} \right) \right)^2} + e^{-2 \left(\pi \sigma_x \left(x_f + \frac{1}{\lambda_x} \right) \right)^2}, \quad (3)$$

where σ_x and λ_x are defined in (2), and x_f is the lateral coordinate in the frequency domain of the RF image.

2.2. Elastography estimator description

2.2.1. Optical flow based Lagrangian speckle model estimator

The OF-based LSME accounts for rigid and non-rigid tissue motions using an affine transformation model, and estimates the displacement and strain in a small region of interest (ROI), also called measurement window (MW). Assuming that the image intensity between two consecutive RF images is not modified in a MW, we can deduce the optical

flow equation for an arbitrary point:

$$I_x U_x + I_z U_z + I_t = 0, \quad (4)$$

where I_x, I_z are the spatial gradient of the image intensity, U_x, U_z represent the lateral and axial displacements, and I_t denotes the temporal gradient of the image intensity.

In a MW, taking a 1st order Taylor expansion of displacements U_x, U_z of an arbitrary point, the affine description of the displacement field is given by

$$U_x(x, z) = U_x(x_0, z_0) + (x - x_0) s_{xx} + (z - z_0) s_{xz}, \quad (5)$$

$$U_z(x, z) = U_z(x_0, z_0) + (x - x_0) s_{zx} + (z - z_0) s_{zz}, \quad (6)$$

where x_0, z_0 are coordinates of the center of the MW, $s_{xx}, s_{xz}, s_{zx}, s_{zz}$ are the lateral strain, lateral shear, axial shear, and axial strain, respectively, and $s_{ij} = \partial U_i / \partial j$.

Since there are two unknown variables in (4), to solve the 2-D optical flow, we assume that the motion field of each pixel within a MW with $p \times q$ pixels is the same and that the coordinates of the center of the MW, x_0, z_0 , are zero. Then, we can rewrite (4) by considering (5) and (6) for each pixel to obtain an over-determined linear equation system for all pixels in a MW,

$$\begin{bmatrix} I_{x_1} x_1 & I_{x_1} z_1 & I_{x_1} & I_{z_1} x_1 & I_{z_1} z_1 & I_{z_1} \\ \vdots & \vdots & \vdots & \vdots & \vdots & \vdots \\ I_{x_{p \times q}} x_{p \times q} & I_{x_{p \times q}} z_{p \times q} & I_{x_{p \times q}} & I_{z_{p \times q}} x_{p \times q} & I_{z_{p \times q}} z_{p \times q} & I_{z_{p \times q}} \end{bmatrix} \begin{bmatrix} s_{xx} \\ s_{xz} \\ U_x \\ s_{zx} \\ s_{zz} \\ U_z \end{bmatrix} = - \begin{bmatrix} I_{t_1} \\ \vdots \\ I_{t_{p \times q}} \end{bmatrix}. \quad (7)$$

Then, solving this equation system using a robust weighted least square method, as described by (4) of [27], the affine motion vector $\vec{m} = (s_{xx}, s_{xz}, U_x, s_{zx}, s_{zz}, U_z)^T$ is obtained. Note that derivatives of displacement are not used to compute strain components.

2.2.2. Affine phase based estimator

Once there are periodic oscillations in axial and lateral directions for a RF image, such as TO images, 2-D motions between consecutive images can be estimated using the APBE method. This estimator is briefly described here; more details are given in [26]. The pre-motion and post-motion images i_1 and i_2 with lateral modulations at consecutive times t_1 and t_2 can be assumed using a 2-D signal model modulated by spatial frequencies f_x and f_z , respectively [29]:

$$i_1(x, z, t_1) = w_1(x, z, t_1) \cos(2\pi f_x x) \cos(2\pi f_z z), \quad (8)$$

$$i_2(x, z, t_2) = w_2(x, z, t_2) \cos(2\pi f_x (x + U_x)) \cos(2\pi f_z (z + U_z)), \quad (9)$$

where w_1 and w_2 are two 2-D windows defined arbitrarily, $f_x = 1/\lambda_x$ and $f_z = 1/\lambda_z$, with λ_x and λ_z defined in (2), and U_x and U_z being lateral and axial components of the displacement, respectively. Note that phases in (8) and (9) do not change when the displacement is equal to one wavelength, thus the largest unbiased estimated displacement is limited to half a wavelength ($\lambda_x/2$ in the lateral direction and $\lambda_z/2$ in the axial direction).

Given the Fourier spectrum of i_1 or i_2 , four single-quadrant analytic signals can be obtained by keeping only one quadrant and canceling other three quadrants. Since the 2-D Fourier transform of real images is symmetric, only two analytic signals were considered. According to [29], the upper left and right quadrants of each spectrum were used. Two-dimensional displacements between consecutive images are associated with phases of analytic signals, as described here:

$$U_x = \frac{\Phi_1 - \Phi_2}{4\pi f_x}, \quad (10)$$

$$U_z = \frac{\Phi_1 + \Phi_2}{4\pi f_z}, \quad (11)$$

with

$$\Phi_1(x, z) = \mathcal{O}_{s11}(x, z, t_1) - \mathcal{O}_{s21}(x, z, t_2), \quad (12)$$

$$\Phi_2(x, z) = \mathcal{O}_{s12}(x, z, t_1) - \mathcal{O}_{s22}(x, z, t_2), \quad (13)$$

where \mathcal{O}_{s11} , \mathcal{O}_{s12} are extracted phases of abovementioned analytical images for the image i_1 , and \mathcal{O}_{s21} , \mathcal{O}_{s22} are phases of analytical images for the image i_2 .

We can do the same process for (10) and (11) as we did for the LSME by introducing an affine model, and then rewriting these two equations for each pixel in a MW with $p \times q$ pixels. The affine APBE model is obtained by combining all equations into a matrix format, as described below in (14) and (15). The similar affine motion vector \vec{m} was obtained by solving this over-determined equation system using the same robust weighted least square method, as we did for the LSME, unlike the classical least square fitting in [26], to provide a common framework of comparison. This constitutes a new contribution to the APBE (new implementation).

$$\begin{bmatrix} x_1 & z_1 & 1 \\ \vdots & \vdots & \vdots \\ x_{p \times q} & z_{p \times q} & 1 \end{bmatrix} \begin{bmatrix} s_{xx} \\ s_{xz} \\ U_x \end{bmatrix} = \frac{1}{4\pi f_x} \begin{bmatrix} \Phi_1(x_1, z_1) - \Phi_2(x_1, z_1) \\ \vdots \\ \Phi_1(x_{p \times q}, z_{p \times q}) - \Phi_2(x_{p \times q}, z_{p \times q}) \end{bmatrix}, \quad (14)$$

$$\begin{bmatrix} x_1 & z_1 & 1 \\ \vdots & \vdots & \vdots \\ x_{p \times q} & z_{p \times q} & 1 \end{bmatrix} \begin{bmatrix} s_{zx} \\ s_{zz} \\ U_z \end{bmatrix} = \frac{1}{4\pi f_z} \begin{bmatrix} \Phi_1(x_1, z_1) + \Phi_2(x_1, z_1) \\ \vdots \\ \Phi_1(x_{p \times q}, z_{p \times q}) + \Phi_2(x_{p \times q}, z_{p \times q}) \end{bmatrix}. \quad (15)$$

2.2.3. Time-ensemble approach

Because of the ultrafast CPWC imaging mode considered in this study, we could implement a time-ensemble approach into the APBE, as done for the LSME in [27]. Specifically, we assumed a constant motion over a given period of time $T = n_t \Delta t$, where n_t is the number of successive frame pairs, and Δt is the time step between two consecutive frames. By combining these frames, the number of linear equations in the least square estimation is increased to $n_t \times n$, where n is the number of pixels in the MW of the estimator. In theory, the more time ensemble is used, better is the robustness of the least square estimation. However, the improvement in strain estimation is at the expense of computational time. For the LSME, we chose a time ensemble number of 8, as it provided the best compromise between accuracy and computational time [27]. For the developed APBE, we assessed estimation errors for different time ensembles (results not shown). We found exponentially decreasing strain estimation errors as a function of the time ensemble numbers. For example, an ensemble number of 12 provided 5% less estimation errors than $n_t = 8$ while increasing by 50% the computation time. Thus, to provide comparable results between APBE and LSME, we used $n_t = 8$ for both strain estimation methods.

2.2.4. Incompressibility constraint for the affine models

Arterial tissue incompressibility is a common assumption used in computational models of arteries [49,50], motion compensation for strain imaging [51], ultrasound speckle tracking [52], angular strain compounding [35,53], and ultrasound modulography [54]. *Ex vivo* analyses have confirmed that arteries may be considered incompressible under physiological conditions [55,56]. Karimi et al. [57] recently showed that both excised healthy and atherosclerotic human coronary arteries are incompressible. The artery tissue is in fact slightly compressible but may be regarded as incompressible at small strains [55], which is attainable by the high frame rate plane wave imaging method used in this study. In addition, as described in Sections 3.1.1 and 3.2.1, we modeled the tissue as isotropic and quasi-incompressible (Poisson's ratio = 0.4995) for vascular simulations. For *in vitro* experiments, two phantoms were built with polyvinyl alcohol cryogel

(PVA-C) following the manufacturing description of [58]. The Poisson's ratio of this material was estimated at 0.499 ± 0.001 , which corresponds to an incompressibility condition [58].

The deformation of an incompressible tissue produces no volume change, which is formulated with the divergence of the displacement field U as $\nabla \cdot U = 0$. Under the condition of 2D plane strain, the out of plane strain component is negligible and the divergence of U can be rewritten as $\nabla \cdot U = \frac{\partial U}{\partial x} + \frac{\partial U}{\partial z} = s_{xx} + s_{zz} = 0$. Consequently, under these assumptions:

$$s_{xx} = -s_{zz}, \quad (16)$$

By introducing (16) into (7) for the LSME, the motion vector \vec{m} is reduced from six to five unknowns, and consequently the minimization process considered the following equation:

$$\begin{bmatrix} I_{x_1 z_1} & I_{x_1} & I_{z_1 x_1} & I_{z_1} z_1 - I_{x_1} x_1 & I_{z_1} \\ \vdots & \vdots & \vdots & \vdots & \vdots \\ I_{x_{p \times q} z_{p \times q}} & I_{x_{p \times q}} & I_{z_{p \times q} x_{p \times q}} & I_{z_{p \times q} z_{p \times q}} - I_{x_{p \times q} x_{p \times q}} & I_{z_{p \times q}} \end{bmatrix} \begin{bmatrix} s_{xz} \\ U_x \\ s_{zx} \\ s_{zz} \\ U_z \end{bmatrix} = - \begin{bmatrix} I_{t_1} \\ \vdots \\ I_{t_{p \times q}} \end{bmatrix}. \quad (17)$$

For the APBE, axial and lateral motion components were computed using (14) and (15), respectively, and then the lateral strain s_{xx} was replaced by the axial strain $-s_{zz}$ when considering this assumption. Other displacement and strain components were assessed during the minimization process and used in these equations. In [27], it was shown that this incompressibility constraint in the LSME reduced the variability of principal strain estimations. In the current study, we aimed improving the quality of principal strain elastograms by also incorporating this constraint into the APBE. Reported results considered APBE and LSME implementations with and without the incompressibility constraint.

2.3. Implementation of elastography estimators and evaluation scheme

We adopted the implementation scheme of [27], which includes 7 steps. Briefly, a rigid registration using 2-D Fourier-based ensemble-correlations [59] was first performed for each small MW between pre- and post-deformed RF images to account for large displacements. Then, the affine motion vector \vec{m} was computed using a weighted least-squares method [60] from registered pre- and post-deformed MWs. For the sake of a fair comparison, the same parameters were used for both estimators (LSME and APBE). Image pixels in a MW were weighted by a 2-D Gaussian function with a FWHM of 1.0×1.0 mm. Thus the MV size was set at 1.3×1.3 mm, which corresponds to 68 samples axially by 26 RF lines laterally, with the same 80% overlap in axial and lateral directions. The spatial discretization of elastograms was thus 0.26×0.26 mm. A 90% overlap in time was chosen for the time-ensemble approach.

We filtered CPWC images to obtain TO images (labeled CPWC&TO). The APBE, the APBE using the time-ensemble approach, and the constrained APBE (*i.e.*, incompressibility constraint) with the time-ensemble approach were tested on CPWC&TO data (we used the following abbreviations (see also Table 1): CPWC&TO + APBE, CPWC&TO + APBE^T and CPWC&TO + APBE^{T&I}). In addition, the LSME using the time-ensemble approach, with or without the incompressibility constraint, was tested with CPWC&TO and CPWC data (described as: CPWC&TO + LSME^T, CPWC&TO + LSME^{T&I}, and CPWC + LSME^{T&I}). The performance of six strategies (image beamforming schemes + estimators) was evaluated with simulations and *in vitro* phantom experiments.

3. Materials and methods

We simulated a heterogeneous vascular model with a mimicking atherosclerotic plaque and fabricated homogeneous vessel wall and heterogeneous phantoms for evaluation. Plane wave data were collected and beamformed using CPWC imaging at 21 angles, which allowed a frame rate of 500 s^{-1} . We used the full aperture to transmit and receive plane waves. Also, a rectangular window apodization function was used for beamforming. The RF images were reconstructed on a regular Cartesian grid (with $50 \times 20 \mu\text{m}$ resolution). CPWC images were then filtered to obtain CPWC&TO images.

3.1. Simulation of a heterogeneous image sequence

3.1.1. Finite element model

A model of a carotid artery with soft and hard inclusions in a cross-sectional view was created using COMSOL Multiphysics (Structural Mechanics Module, version 3.5, COMSOL, France). The plaque geometry described in [61] was meshed with approximately 15,000, 6-node triangular elements. To avoid translations and rotations of the rigid body, a soft and compressible (elasticity modulus $E = 1 \text{ Pa}$ and Poisson's ratio $\nu = 0.001$) layer of 1 mm thickness was added on the outer layer. This artificial outer contour was anchored and was not considered in the elastography analysis. As reported, a wide range of Young's moduli, varying from 30 kPa to 270 MPa, for *ex vivo* or *in vivo* atherosclerotic tissues has been reported in the literature, depending on plaque internal structures and measurement methods [62]. In this study, a large soft necrotic core ($E = 10 \text{ kPa}$) was embedded in a medium mimicking a fibrous plaque ($E = 600 \text{ kPa}$). Four calcified inclusions ($E = 5000 \text{ kPa}$) were also embedded within the plaque. The Poisson's ratio of all plaque components considered isotropic was fixed at 0.4995 (*i.e.*, incompressible). These mechanical parameters are close to those used in [63,64]. Recently, similar parameters were also selected for elasticity reconstruction methods [54,65,66]. Displacements of the vessel wall between two successive image frames were computed using the finite element method (FEM). To consider realistic dynamic conditions, a systemic blood pressure waveform with minima and maxima at 80 and 120 mmHg (10 and 16 kPa) was applied to the simulated geometry. This waveform was discretized with 500 samples to simulate an ultrafast non-invasive ultrasound acquisition at a frame rate of 500 s^{-1} . The strain field was derived under plane strain conditions from computed displacement fields.

3.1.2. Acoustic models

The ultrasound simulation program Field II [67] was used to obtain RF images coupled with FEM simulated wall motions. The L14-5/38 linear array probe with 128 elements (Ultrasonix Medical Corporation, Richmond, BC, Canada) was simulated by considering a 7.2 MHz center frequency, a 70% fractional bandwidth (at -6 dB) and a sampling rate of 40 MHz. The bandwidth of that probe is between 5 and 14 MHz. The central frequency of 7.2 MHz allowed good resolution and acceptable grating lobes when using CPWC imaging [41]. The abovementioned vascular model included randomly distributed scatterers whose density was 100 per resolution cell [68] in a cross-sectional view. For CPWC beamforming, the full aperture was activated in transmission to create plane waves. The vascular model was static during emission angles changing from -10° to 10° . The plane wave data with different steering angles were beamformed and compounded to form pre-deformation images using the delay-and-sum algorithm [41]. To form post-deformation images, the displacement fields generated by the FEM were applied on this model and the plane wave data on the deformed model were beamformed and compounded using the same steering angles. The CPWC image sequence was filtered to generate CPWC&TO images. All beamformed images were contaminated with white Gaussian noise at a SNR of 20 dB.

3.2. In vitro experiment description

3.2.1. Phantom fabrication

Two phantoms were built following the manufacturing description in [58]. The solution had a concentration of 10% by weight of polyvinyl alcohol dissolved in pure water and ethanol homopolymer. The weight percentage of added particles used as acoustic scatterers (Sigmacell cellulose, type 50, Sigma Chemical, St Louis, MO, USA) was 3%. The homogeneous phantom consisted in a 6 freeze-thaw cycles polyvinyl alcohol cryogel (PVA-C) material. The second phantom was constructed to mimic a heterogeneous vascular wall with a soft inclusion. The outer PVA-C layer was fabricated with 6 freeze-thaw cycles and the soft inclusion mimicking a lipid pool underwent 1 freeze-thaw cycle. The first homogeneous phantom without any inclusion had a modulus of $182 \pm 21 \text{ kPa}$ as measured by tensile test [58]. The heterogeneous phantom with a soft inclusion had a modulus of $25 \pm 3 \text{ kPa}$ [58], with the surrounding material at $182 \pm 21 \text{ kPa}$.

3.2.2. Experimental setup

The experimental setup is analog to that illustrated in Fig. 2 of [27]. The intra-luminal pressure was monitored (Vivitro Labs Inc., Victoria, BC, Canada) and varied using a pulsatile pump (model 1421, Harvard Apparatus, Holliston, MA). Peak and minimum pressures were set at 120 and 60 mmHg, respectively, and an image sequence was acquired. To test the robustness of the different elastography estimators to different strains, the image sequence was down sampled using different time steps to produce frame rates from 500 s^{-1} to 9 s^{-1} .

3.2.3. Ultrasound data acquisition

Cross-sectional RF images were acquired with a Sonix Touch ultrasonic system (Ultrasonix Medical Corp.) equipped with a linear array probe of 128 elements (L14-5/38). Plane wave ultrafast data at different steering angles were stored on the Sonix DAQ multi-channel system. A software development kit (TexoSDK, v6.0.1, Ultrasonix Medical Corp.) was used to generate and record plane wave data. Beamforming was performed in post-processing.

3.3. The choice of TO filtering parameters

As described in (3), the frequency pattern of the image formed by a TO filter is determined by two parameters, the expected lateral oscillation wavelength λ_x and the FWHM of the Gaussian envelope σ_x . Intuitively, smaller are λ_x and σ_x , wider is the spectrum of the filtered image and higher is the lateral TO frequency. However, too small λ_x and σ_x will filter most energy of the image and may induce the filter to only keep the noise. As a result, the proper TO filtering parameters λ_x and σ_x were determined via a simple simulation test. Two successive frames was selected from the simulated image sequence described in Section 2.1 with a SNR of 20 dB. Different values of λ_x and σ_x were tested on this image pair 50 times. Parameters providing the least deviation between ground true FEM and computed elastograms were chosen for TO filtering in the remaining of this study. Considering the spectrum of compounded images and the window size of estimators, we set the test range of λ_x from 0.4 to 1 mm and that of σ_x from 0.2 to 1 mm, with increments of 0.1 mm.

3.4. Data analysis

3.4.1. Principal strain

The Cartesian strain tensor was transformed into the principal minor and major strain tensors, ϵ_{min} , ϵ_{max} , by using the following expression [69]:

$$\epsilon_{min,max} = \frac{s_{xx} + s_{zz}}{2} \pm \sqrt{\left(\frac{s_{xx}-s_{zz}}{2}\right)^2 + \left(\frac{s_{xz} + s_{zx}}{2}\right)^2}, \quad (18)$$

where s_{xx} , s_{zz} are lateral and axial strains, and s_{xz} , s_{zx} are corresponding shear components. When we used the incompressibility constraint, the lateral strain component s_{xx} was replaced by $-s_{zz}$ in this equation.

In this study, otherwise specified, the principal strain map between consecutive frames was estimated for an image sequence. Then, principal strains were cumulated over the range of pressure considered. The largest cumulated strain map was chosen as the final elastogram.

3.4.2. Elastogram evaluation

To evaluate simulated elastograms, the normalized root-mean-square-error (NRMSE) between FEM and estimated principal strains was used:

$$NRMSE = \sqrt{\frac{\sum_{j=1}^N (ref_j - est_j)^2}{N}} \cdot \frac{1}{ref_{max} - ref_{min}}, \quad (19)$$

where N is the number of pixels in an elastogram, ref is the ground truth principal strain from the finite element analysis, and est is the estimated strain from LSME or APBE algorithm.

Since the ground truth strain value is unknown for *in vitro* experiments, we chose the SNR as the evaluation metric of elastograms for homogeneous and heterogeneous phantoms. The CNR was also used for the evaluation of elastograms of the heterogeneous phantom.

$$SNR = 10 \log \left(\frac{\mu_{r1}}{\sigma_{r1}} \right) + 10 \log \left(\frac{\mu_{r2}}{\sigma_{r2}} \right), \quad (20)$$

$$CNR = 10 \log \left(\frac{2(\mu_{r1} - \mu_{r2})^2}{\sigma_{r1}^2 + \sigma_{r2}^2} \right). \quad (21)$$

Here, μ_{r1}, μ_{r2} and σ_{r1}, σ_{r2} are means and standard deviations of cumulated principal strains in selected ROIs 1 and 2.

4. Results

4.1. Optimal TO filtering parameters

The test results on TO filtering parameter selection using different pairs of λ_x and σ_x are represented in Fig. 1(a). The smallest estimation deviation for principal strains was obtained for $\lambda_x = 0.5$ mm and $\sigma_x = 0.4$ mm. These values were used in the remaining of this study. Fig. 1(b) presents the corresponding filtering mask as described by (3).

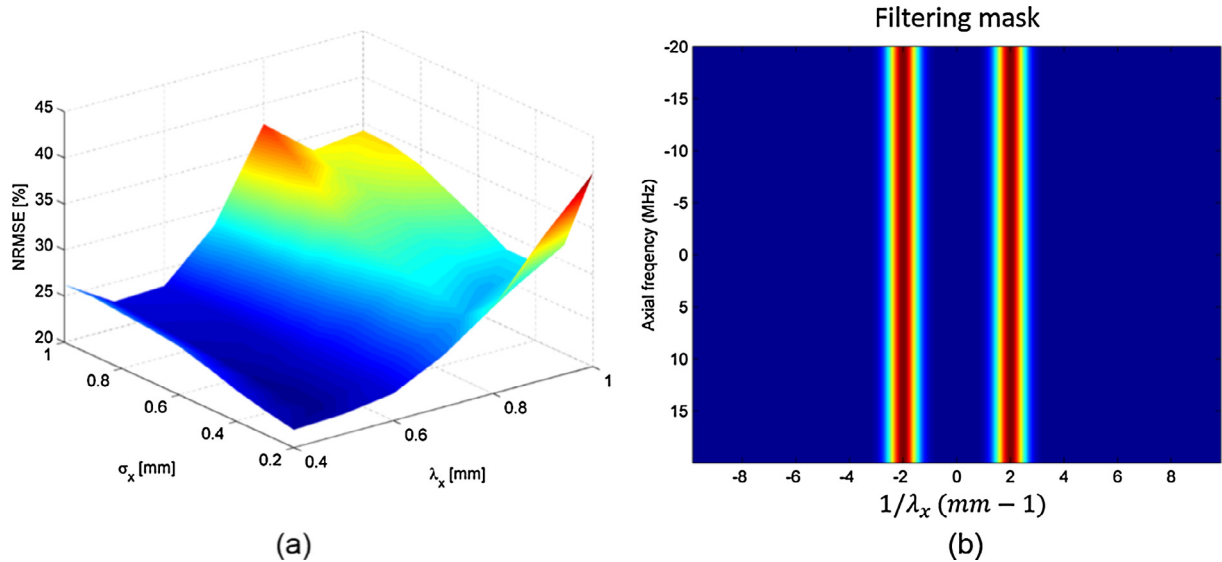


Fig. 1. (a) The choice of TO filtering parameters using different pairs of λ_x and σ_x . Here the test range of λ_x is from 0.4 mm to 1 mm and that for σ_x is from 0.2 mm to 1 mm, with 0.1 mm increment. From this simulation, $\lambda_x = 0.5$ mm and $\sigma_x = 0.4$ mm provided the smallest estimation deviation (NRMSE) for principal strains and these values were chosen as the TO filtering parameters in our study. (b) The corresponding filtering mask.

4.2. The heterogeneous vessel simulation study

Fig. 2(a) and (b) shows B-mode images of the heterogeneous artery simulation considering CPWC and CPWC&TO beamforming. Principal minor strains obtained with six configurations (CPWC&TO + APBE, CPWC&TO + APBE^T, CPWC&TO + APBE^{T&I}, CPWC&TO + LSME^T, CPWC&TO + LSME^{T&I} and CPWC + LSME^{T&I}) are shown in Fig. 2(d)–(i), respectively. We chose in Fig. 2(d) the time-ensemble length $n_t = 1$ (i.e., no time-ensemble) for the APBE tested on CPWC&TO data (CPWC &TO + APBE), whereas $n_t = 8$ for other five configurations (as described in Section 2.2.3). Visually, Fig. 2(e) presents less estimation errors than Fig. 2(d), which suggests that the time-ensemble approach improved the estimation accuracy of the APBE. Around 12 and 8 o'clock (outside soft and hard inclusions), the principal minor strain is expected to decrease with radial distance from the lumen, which is known as the strain decay phenomenon [70]. The strain decay is difficult to appreciate from Fig. 2(d)–(f). Quantitatively, the APBE with the incompressibility constraint and using the time-ensemble approach tested on CPWC images with TOs (Fig. 2(f)) provided the smallest estimation error (NRMSE = 10.6%) when compared with the APBE with the time-ensemble approach tested on CPWC images with TOs, CPWC&TO + APBE^T (Fig. 2(e), NRMSE = 13.0%) and the APBE tested on CPWC images with TOs, CPWC&TO + APBE (Fig. 2(d), NRMSE = 14.2%), which confirms that the combination of the time-ensemble approach and incompressibility constraint improved the performance of the APBE. With the LSME, the principal minor strains in Fig. 2(g)–(i) provided more homogeneous and clear outlines of the soft inclusion than APBE elastograms. Moreover, the strain decay at 12 and 8 o'clock is observed. The performance of the LSME, with and without the incompressibility constraint, tested on CPWC images with and without TOs (CPWC&TO + LSME^T, CPWC&TO + LSME^{T&I} and CPWC + LSME^{T&I}) is overall comparable, with NRMSE at 9.0%, 8.6% and 8.4%, respectively.

Regarding the principal major strain, the same conclusions apply. The APBE with the time-ensemble approach (Fig. 2(l)) showed less estimation artifacts than APBE without time averaging (Fig. 2(k)). However, both panels (k) and (l) did not delineate properly the soft inclusion around 4 to 6 o'clock. With the incompressibility constraint (panel (m)), the outline of the soft inclusion was better depicted. The NRMSE confirmed those visual observations; normalized errors were 17.4%, 14.5% and 12.9% for panels (k)–(m), respectively. With the

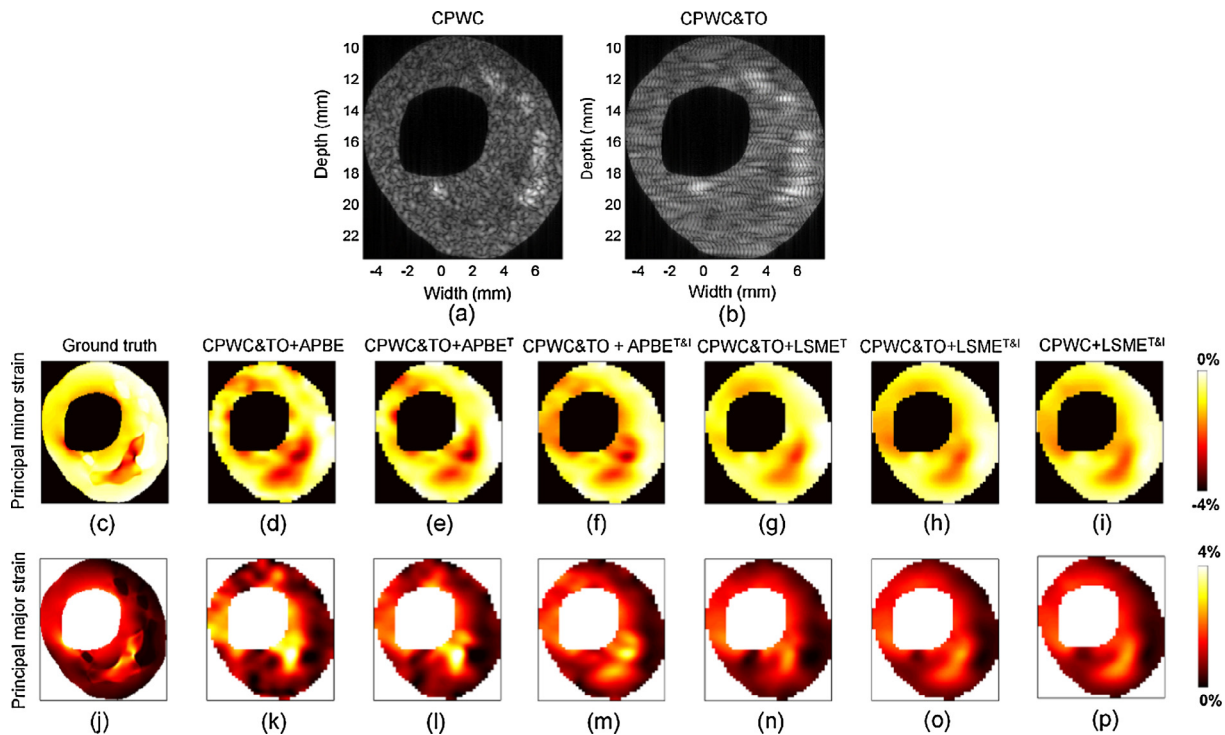


Fig. 2. B-mode images and principal strains for a simulated vascular phantom with one soft inclusion and four hard inclusions. First row: the CPWC image and CPWC &TO image. Second row: ground truth of the principal minor strains from finite-element model and the principal minor strain estimated with the APBE on CPWC&TO data, the APBE using the time-ensemble approach on CPWC&TO data, the APBE using the incompressibility constraint and the time-ensemble approach on CPWC&TO data, the LSME using the time-ensemble approach on CPWC&TO data, the LSME using the incompressibility constraint and the time-ensemble approach on CPWC &TO data, and the LSME using the incompressibility constraint and the time-ensemble approach on CPWC data, whose NRMSE are 14.2%, 13.0%, 10.6%, 9.0%, 8.6%, 8.4%, respectively. Third row: ground truth of the principal major strains from finite-element model and the principal major strain estimated with the APBE and LSME using the same strategies, whose NRMSE are 17.4%, 14.5%, 12.9%, 9.6%, 9.4%, and 9.5%, respectively.

LSME, the incompressibility constraint, CPWC&TO + LSME^{T&I} (Fig. 2(o)) and CPWC + LSME^{T&I} (Fig. 2(p)), allowed better outlines of the soft inclusion than the implementation without this constraint, CPWC&TO + LSME^T (Fig. 2(n)). LSME provided better results compared with the three APBE implementations, with NRMSE at 9.6% (panel (n) with TO beamforming), 9.4% (panel (o) with TO beamforming), and 9.5% (panel (p) with no TO), respectively.

4.3. In vitro experiments

4.3.1. The homogeneous vascular phantom study

Fig. 3(a)–(c) shows a picture, and cross-sectional CPWC and CPWC with TOs B-mode images of the homogeneous phantom without any inclusion. As done for the simulation study, the following description compares principal strains of six APBE and LSME implementations. APBE results in panels (d)–(f) confirmed the simulation study. Indeed, the time-ensemble approach and incompressibility constraint improved principal minor strain estimates but several artifacts are noticed on those elastograms. More consistent estimates were obtained with the LSME. The strain decay phenomenon is clearly seen in panels (g)–(i). Visually, a more homogeneous strain texture was obtained with the LSME that considered the time-ensemble and incompressibility constraint, and CPWC beamforming (*i.e.*, the implementation of [27], see panel (i)). To evaluate quantitatively the performance of those implementations, two regions of interest were selected to calculate the SNR (dashed green lines in Fig. 3(i)). One was selected as a 4-mm radius circle surrounding the lumen, whereas the other was an arc from 3 to 8 o'clock 5 mm away from the lumen center. SNRs in Fig. 3(d)–(i) are 11.1 dB, 11.3 dB, 12.0 dB, 15.9 dB, 14.2 dB and 16.5 dB, respectively. The best SNR was obtained with the implementation of the LSME with the time-ensemble and incompressibility constraint on CPWC data

(CPWC + LSME^{T&I}).

Regarding principal major strains of Fig. 3(j)–(o), visual observations are similar to those reported for principal minor strain elastograms. Overall, artifacts are observed on all strain maps and transverse oscillation beamforming seemed to emphasize the variance of both APBE and LSME estimators. With TO, the implementation of the incompressibility constraint (Fig. 3(l) and (n)) provided more consistent estimation at 5 o'clock compared with cases without that constraint (Fig. 3(k) and (m)). The best result was obtained with the LSME with the time-ensemble and incompressibility constraint on CPWC data, as confirmed by SNR results. On panels (j)–(o), SNRs are 7.2 dB, 7.5 dB, 12.0 dB, 8.9 dB, 14.2 dB and 16.5 dB, respectively.

Fig. 4 presents the SNR analysis on principal strains for a wide range of applied strains (from 0.07% to 4.5%). Those results are confirming observations of Fig. 3 on cumulated strain maps at a frame rate of 500 s⁻¹. Except for the highest strain of 4.5%, CPWC beamforming with LSME considering the time-ensemble and incompressibility constraint provided the best SNRs. The worse performance was obtained with APBE on CPWC images with TOs (CPWC&TO). The time-ensemble approach and incompressibility constraint improved SNRs of principal strains for both APBE and LSME. Especially, as seen in Fig. 4(b), all implementations of the incompressibility constraint provided higher SNRs for principal major strains than implementations without that constraint. Differences in performance tended to decrease as the applied strain was increased.

4.3.2. The heterogeneous phantom study

Fig. 5 shows visual assessment of the heterogeneous phantom with a soft inclusion under the lumen, B-mode images using both beamforming approaches, and cumulated principal strain maps. Regarding principal minor strains, fewer artifacts are seen when the time-ensemble and then

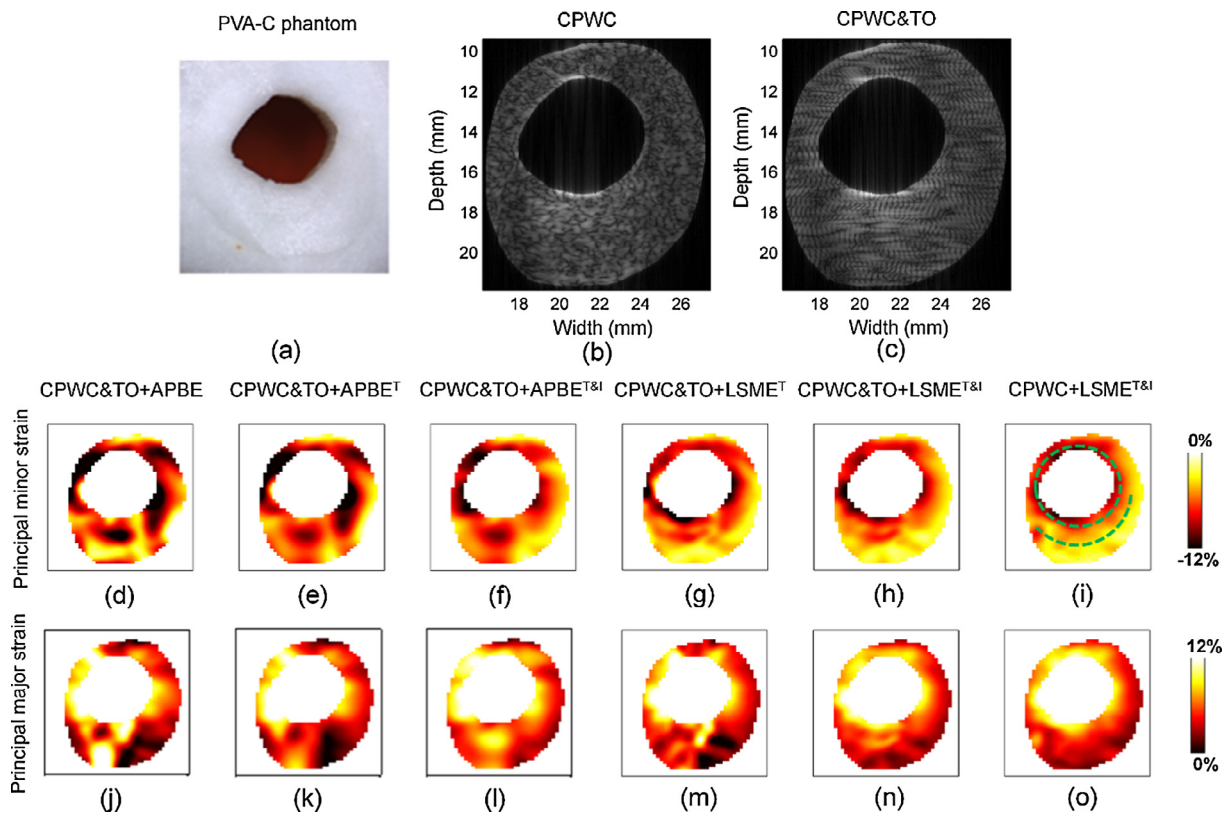


Fig. 3. B-mode images and principal strains of a homogeneous phantom *in vitro* experiment. First row: the cross-section image of the phantom, the CPWC image and CPWC&TO image. Second row: the principal minor strains estimated with the APBE on CPWC&TO data, the APBE using the time-ensemble approach on CPWC&TO data, the APBE using the incompressibility constraint and the time-ensemble approach on CPWC&TO data, the LSME using the time-ensemble approach on CPWC&TO data, the LSME using the incompressibility constraint and the time-ensemble approach on CPWC&TO data, and the LSME using the incompressibility constraint and the time-ensemble approach on CPWC data, whose SNRs are 11.1 dB, 11.3 dB, 12.0 dB, 15.9 dB, 14.2 dB, 16.5 dB respectively. Third row: the principal major strains estimated with the APBE and LSME using the same strategies, whose SNRs are 7.2 dB, 7.5 dB, 12.0 dB, 8.9 dB, 14.2 dB, and 16.5 dB, respectively.

the incompressibility constraint were added to the APBE estimator. When compared with LSME implementations (panels (g)–(i)), more deformations are noticed within the soft inclusion for the different APBE estimates (panels (d)–(f)). In general, with the exception of a few artifacts at 3 o’clock, the soft inclusion was well delineated with LSME

implementations. Some overestimation of the inclusion dimension is nevertheless noticed with the LSME implementation on CPWC data (CPWC + LSME^{T&I}). For quantitative analyses, 5 small rectangles of 0.5 mm × 0.5 mm with the same distance away from the lumen center were selected (see white ROIs and the manual segmentation of the

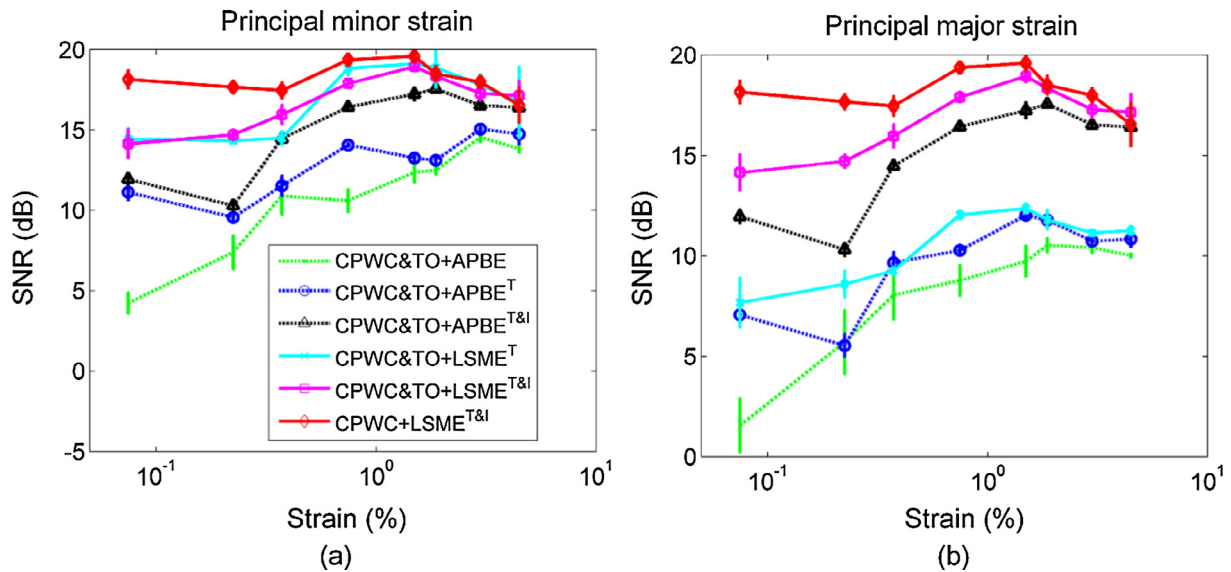


Fig. 4. SNRs calculated from principal strains estimated with CPWC&TO + APBE, CPWC&TO + APBE^T, CPWC&TO + APBE^{T&I}, CPWC&TO + LSME^T, CPWC&TO + LSME^{T&I}, and CPWC + LSME^{T&I} over a range of applied strains from 0.07% to 4.5%. (a) Principal minor strains. (b) Principal major strains. Five realizations were considered.

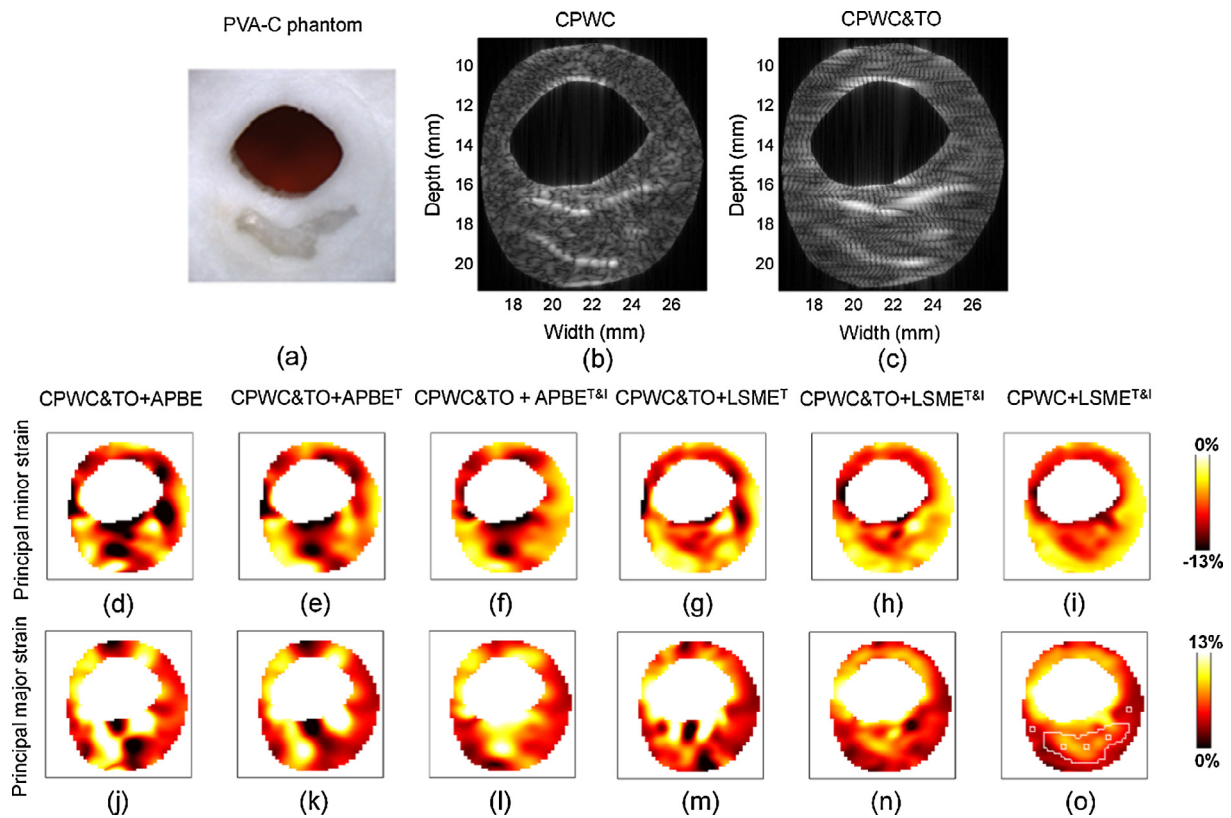


Fig. 5. B-mode images and principal strains of a heterogeneous phantom *in vitro* experiment. First row: the cross-section image of the phantom, the CPWC image and CPWC&TO image. Second row: the principal minor strains estimated with the APBE on CPWC&TO data, the APBE using the time-ensemble approach on CPWC&TO data, the APBE using the incompressibility constraint and the time-ensemble approach on CPWC&TO data, the LSME using the time-ensemble approach on CPWC&TO data, the LSME using the incompressibility constraint and the time-ensemble approach on CPWC&TO data, and the LSME using the incompressibility constraint and the time-ensemble approach on CPWC data, whose SNRs are 7.6 dB, 9.5 dB, 18.3 dB, 12.5 dB, 19.4 dB, and 21.1 dB, respectively, and CNRs are -5.2 dB, 4.1 dB, 10.2 dB, -2.6 dB, 11.5 dB, and 16 dB, respectively. Third row: the principal major strains estimated with the APBE and LSME using the same strategies, whose SNR are 9.7 dB, 11.5 dB, 18.3 dB, 12.6 dB, 19.4 dB, and 21.1 dB, respectively, and CNRs are -8.5 dB, 0.4 dB, 10.2 dB, 3.2 dB, 11.5 dB, and 16 dB, respectively.

inclusion on panel (o)). Three ROIs were chosen within the soft inclusion that was manually segmented from B-mode images to calculate the SNR. The two others were selected out of the soft inclusion to calculate the CNR together with the above three ROIs. SNRs from left to right in Fig. 5(d)–(i) were 7.6 dB, 9.5 dB, 18.3 dB, 12.5 dB, 19.4 dB and 21.1 dB, respectively. CNRs were -5.2 dB, 4.1 dB, 10.2 dB, -2.6 dB, 11.5 dB and 16 dB, respectively. According to SNR and CNR results, the best implementation is with the LSME considering the time-ensemble and incompressibility constraint on CPWC-beamformed data (*i.e.*, the benchmark reference of [27]).

Regarding principal major strains, similar to previous results, all APBE implementations with CPWC&TO beamforming did not allow identifying the soft inclusion precisely. A lot of artifacts are also noticed with the LSME tested on CPWC&TO images when the incompressibility constraint was ignored (panel m). With the incompressibility constraint, the LSME provided clearer depiction of the inclusion (panels n and o). SNRs in Fig. 5(j)–(o) were 9.7 dB, 11.5 dB, 18.3 dB, 12.6 dB, 19.4 dB and 21.1 dB, respectively. CNRs were -8.5 dB, 0.4 dB, 10.2 dB, 3.2 dB, 11.5 dB and 16.0 dB, respectively. Again, the LSME with the time-ensemble and incompressibility constraint with CPWC beamforming provided the best results among all implementations.

SNR and CNR analyses of elastograms over different applied strains, from 0.07% to 3.6%, are given in Fig. 6. Overall, results are consistent with the visual observation of Fig. 5. LSME configurations considering the time-ensemble and incompressibility constraint applied on CPWC images with (CPWC&TO + LSME^{T&I}) and without TOs (CPWC + LSME^{T&I}) still provided the highest SNRs and CNRs. Principal strains from the APBE with the time-ensemble and incompressibility constraint on

CPWC images with TOs (CPWC&TO + APBE^{T&I}) had higher SNRs and CNRs than the other two APBE implementations, which confirms again that the time-ensemble and incompressibility constraint improve the performance of this estimator. Similar to Fig. 4(b), configurations considering the incompressibility constraint (CPWC&TO + APBE^{T&I}, CPWC&TO + LSME^{T&I} and CPWC + LSME^{T&I}) presented higher SNRs for principal major strains. With a few exceptions, CNRs were also higher for both principal minor and major strains when the incompressibility constraint was used (Fig. 6(c) and (d)). Except for the minimum strain of 0.07%, at 500 images per second, and the maximum strain of 3.6%, transverse oscillation beamforming improved the performance of the LSME in terms of SNRs and CNRs for this specific phantom.

5. Discussion

The APBE proposed in [26] was applied on sectorial cardiac images of standard focusing with TOs. Although an affine model that could directly provide access to the deformation matrix was introduced, radial, circumferential and longitudinal strains were computed from the derivative of the displacement field. In the current study, we adapted the APBE for vascular applications by introducing a time-ensemble approach and an incompressibility constraint to directly assess deformations (no derivatives). The new APBE was shown to provide better strain estimations than the APBE implementation without time ensemble and incompressibility with simulations and *in vitro* experiments. Moreover, we combined CPWC and TO beamforming to obtain CPWC&TO images. The higher frame rate of CPWC&TO imaging compared with

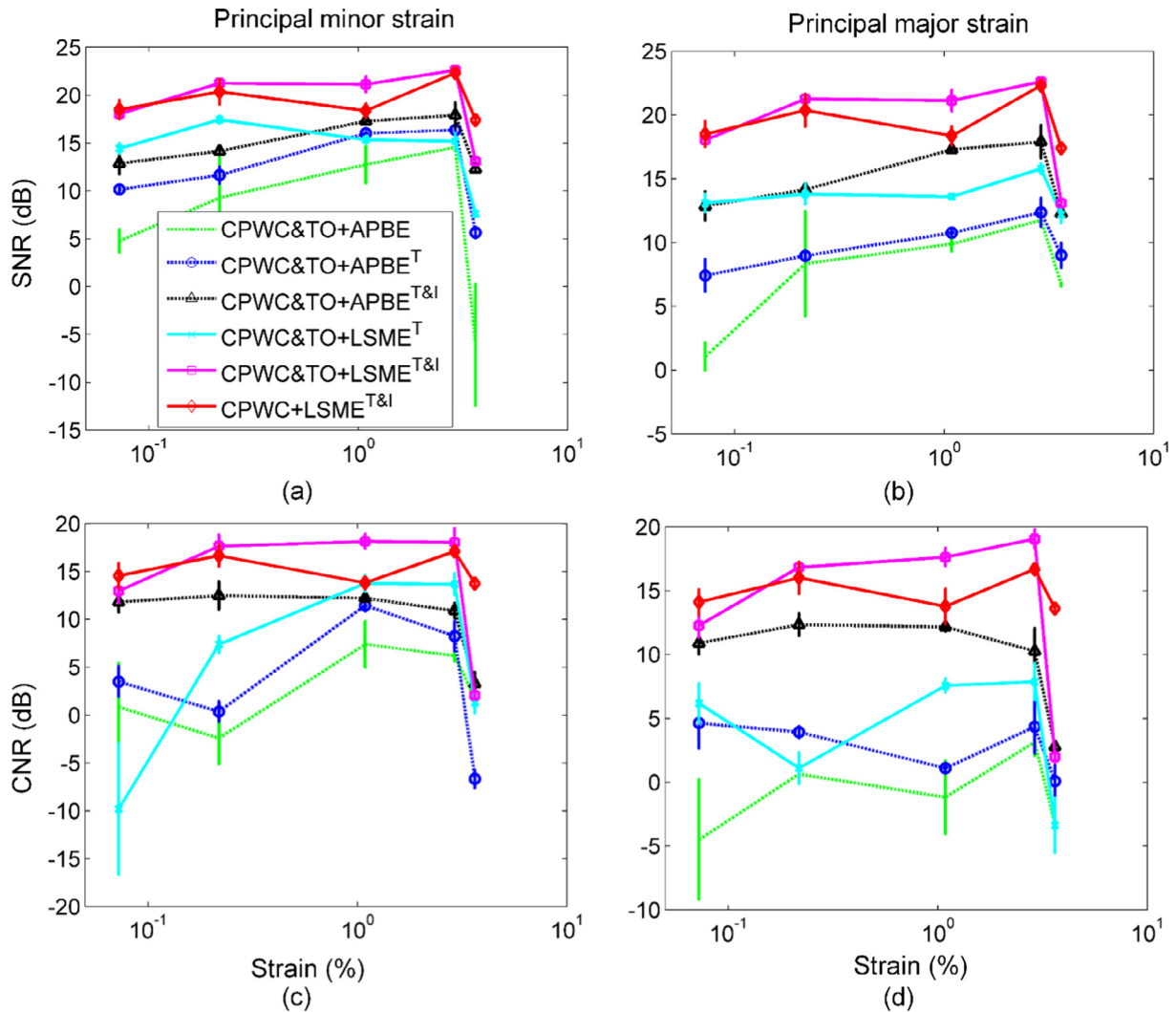


Fig. 6. SNRs and CNRs calculated from principal strains estimated with CPWC&TO + APBE, CPWC&TO + APBE^T, CPWC&TO + APBE^{T&l}, CPWC&TO + LSME^T, CPWC&TO + LSME^{T&l}, and CPWC + LSME^{T&l} over a range of applied strains from 0.07% to 3.6%. (a) and (b) SNRs for principal strains. (c) and (d) CNRs for principal strains. Five realizations were considered.

standard focusing imaging used in [26] provided smaller displacements between consecutive frames, which is an advantage since displacements must be smaller than half a wavelength for unbiased estimations with the APBE, as explained in Section 2.2.2.

In addition, we evaluated the performance of the developed APBE against LSME. Two of the three LSME implementations (CPWC&TO + LSME^{T&l} and CPWC + LSME^{T&l}) outperformed the new APBE (CPWC&TO + APBE^{T&l}) with simulations and *in vitro* experiments. CPWC + LSME^{T&l} provided better strain estimations than CPWC&TO + LSME^{T&l} for homogeneous phantom experiments; but comparable or worse performance for simulations of the heterogeneous vessel or for the heterogeneous phantom depending on strain values.

5.1. Influence of TO filtering on the quality of CPWC images

From simulations and *in vitro* results, as mentioned above, the APBE did not perform better than the LSME. TO filtering may be one of the reasons for that. Firstly, although TO filtering increases lateral textures of an image to facilitate lateral strain estimation, the filtering method used to create TOs is at the expense of losing in lateral resolution. Considering the point spread function (PSF) of a CPWC image (see Fig. 7(a)), we used (3) as a mask to multiply this spectrum to produce a PSF with TOs. This process is also viewed as a convolution of the PSF

with a Gaussian function having two peaks modulated by λ_x and σ_x . The lateral width of the resulting PSF with TOs is expanded due to this Gaussian function convolution (see Fig. 7(b)). Moreover, TO filtering elevates the side lobe level despite narrowing the main lobe width.

Secondly, a CPWC image can be viewed as a wide band signal in the lateral direction from a Fourier spectrum analysis (see Fig. 7(c)). When the CPWC image is filtered by the band pass TO filter, the CPWC&TO image becomes a narrow band signal in the lateral direction (see Fig. 7(d)). The CPWC&TO spectrum is also subdivided from 2 to 4 main components, and as a consequence the spectral magnitude at given 2-D frequencies is reduced, which may violate the phase constancy assumption of the APBE, leading to less accurate strain estimations.

Likewise, the increased beam width and reduced spectrum magnitude of filtered TO images also violate the intensity constancy assumption of the LSME inducing less accurate estimations (see performances of CPWC&TO + LSME^T or CPWC&TO + LSME^{T&l} versus CPWC + LSME^{T&l} for the homogeneous phantom results of Fig. 4). However, the increased lateral oscillations improve image gradients, which was beneficial for the LSME as comparable (Fig. 2) and even better (Fig. 6) performances were obtained when comparing CPWC&TO + LSME^{T&l} with CPWC + LSME^{T&l} when the tissue structure was complex and heterogeneous.

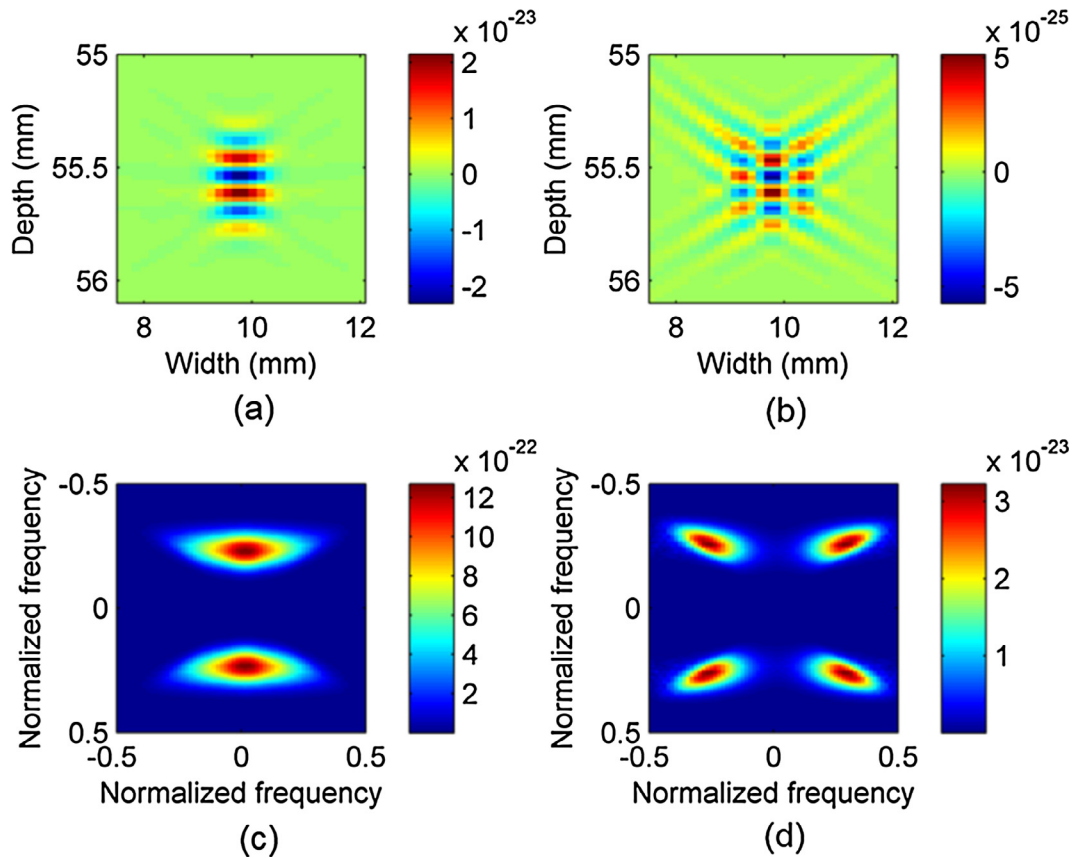


Fig. 7. The point spread functions (PSF) and corresponding Fourier spectra of CPWC and CPWC&TO beamforming: (a) The PSF of the CPWC image, (b) the PSF of the CPWC&TO image, (c) the Fourier spectrum of (a), (d) the Fourier spectrum of (b).

5.2. Influence of the affine model on the APBE

The APBE implemented without an affine model and known as the PBE was shown to be able to track accurately 2D and 3D trajectories with simulated and *in vitro* data [28,45,71]. The APBE proposed by others improved the lateral displacement estimation but provided a slightly less precise axial displacement measurement than the PBE [26]. One possible reason reported in the latter study [26] is that the affine model is more complex and is more prone to over-fitting than the simple PBE model in the presence of noise. Likewise, the same reason may apply to strain estimations with the APBE in our study, which included a minimization process to assess all displacement and deformation components simultaneously. Although the affine model has a low bias due to a precise description of the tissue motion, the increasing model complexity may also bring a high variance in the presence of noise, as discussed earlier when interpreting the performance of CPWC & TO images.

5.3. Bias and variance of the two strain estimators

We hypothesize that the LSME providing better performance than the APBE could be due to the estimation variance. In the supervised learning field [72], the mean-squared error of a model prediction can be decomposed into the noise, the bias and the variance in the form: $MSE = noise + bias^2 + variance$. The noise term is the inherent noise that cannot be reduced. The bias term is referred to how far the prediction is from the true value. The variance term is how much the prediction varies over multiple realizations of the model. Regarding the LSME versus APBE, the maximum detectable displacement in one direction with the APBE is half the wavelength of the oscillations in that direction [71]. The estimation bias of the LSME is also related to the

range of displacements. To better clarify this issue, two simple 1-D versions of APBE (phase-based) and LSME (optical flow-based) methods were used to estimate displacements between a pair of 1-D sinusoids under ideal condition (*i.e.*, no noise). The performance for different displacements is presented in Fig. 8. As seen, the optical flow LSME method can be viewed as a biased estimator [73], whereas the phase-based APBE method is able to provide unbiased estimations until the true displacement becomes less than half a wavelength [29]. When the true displacement is more than half a wavelength, the phase estimator

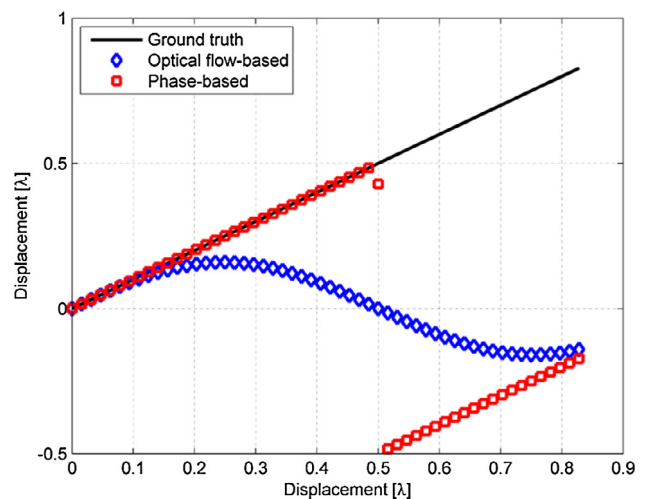


Fig. 8. Performance of the phase-based and optical flow-based estimators to estimate the displacement between a pair of 1-D sinusoidal signals under ideal condition (no noise added) for different displacements along x and y axes.

provides aliased results. As also seen in Fig. 8, when the motion between consecutive frames is small enough (typically less than 0.2λ) to be tractable using CPWC imaging, the bias of the LSME is small. Introducing a small bias into an estimator can reduce the estimation variance leading to an overall lower mean-squared error [74]. Therefore, we hypothesize that the reduced variance may account for the better performance of the LSME versus APBE.

Besides abovementioned possible reasons for the poorer performance of the APBE with TO beamforming, we also investigated the impact of heterodyning demodulation to see if this approach, instead of the frequency domain filtering strategy used to produce lateral oscillations, could improve strain results. Readers are referred to the Appendix A for more details.

5.4. Clinical value of this work

The second most common death cause is stroke accounting for about 1 of 10 deaths in the world [75]. Stroke is mainly induced by atherosclerotic plaque rupture [76]. A prone-to-rupture plaque is usually composed of a large lipid core covered by a thin fibrous cap [77]. In this study, a heterogeneous phantom with a soft inclusion was fabricated to simulate a pathological vulnerable condition. Two of the tested configurations (CPWC&TO + LSME^{T&I} and CPWC + LSME^{T&I}) revealed the existence of the soft inclusion, as identified by large deformations on principal minor strain (Fig. 5(h) and (i)) and principal major strain (Fig. 5(n) and (o)) maps. For the homogeneous phantom (Fig. 3(a)), the anticipated strain decay was noticed on elastograms (Fig. 3 (h), (i), (n), (o)). Thus, we can confirm that the proposed incompressibility constraint and time-ensemble approach with CPWC and CPWC&TO configurations may help identifying features of vulnerable plaques (soft inclusion) and the strain decay of normal vessel walls.

5.5. Limitations and perspectives

Lateral estimations (lateral strain and shear) of LSME and APBE were not as good as axial estimates due to the lower lateral resolution in ultrasound imaging. Because of the deleterious impact of this fact on principal strains, we used the incompressibility constraint to avoid using lateral strain estimates for some tested conditions. Nevertheless, we considered the lateral shear estimation that likely deteriorated the performance of both estimators. High resolution imaging approaches (e.g., minimum variance beamforming [40,78]) may be helpful to

Appendix A

A.1. Impact of heterodyning demodulation on strain performance of the APBE

The heterodyne demodulation has been shown recently to increase the lateral frequency and reduce the lateral beamwidth of the TO method [79,80]. We thus applied this technique to see if it could also improve the performance of the APBE. We decomposed the APBE method to fit two heterodyning images whose oscillations are orthogonal. Specifically, only one quadrant of the spectrum of one analytic signal of the heterodyning demodulation was used. The strain components were derived using the affine model as we did in Section 2.2.2. The optimal parameters of TO images obtained with the heterodyne demodulation were also obtained using successive frames of the simulated carotid image sequence, which are $\lambda_x = 0.5$ mm and $\sigma_x = 0.3$ mm. Strain results are shown in Fig. A1. For these examples only, displacement and strain components without the incompressibility constraint are shown instead of principal strains to better appreciate the influence of the heterodyne demodulation on each motion component. The time ensemble approach was used.

As seen in Fig. A1, no improvements are observed for the APBE when using the heterodyne demodulation. Two reasons may account for this. Firstly, the APBE may not benefit from the double oscillation frequency attributed to the heterodyne demodulation. This may be because the APBE is different from the phased-based zero crossing method in which a higher phase slope is helpful to locate the peak of the complex correlation function. The APBE is directly applied to analytic signals, which do not require a higher oscillation frequency to enable a higher phase slope. Secondly, the APBE was developed in the framework of RF data demodulated in each direction (as for TO images). The heterodyne demodulation decomposes a TO image into a lateral oscillation image and an axial oscillation image, which correspond to two RF images. For each of them, only two analytical phases are used instead of four, as it is done for TO filtered images. The APBE has to derive axial and lateral estimations from axial and lateral demodulated images, respectively. The absence of modulation in one direction has an influence on the accuracy in the other direction (roughly 20% increase in errors compared with TO images) [28].

Although we found that the heterodyne demodulation did not improve the performance of APBE, it does not contradict conclusions of [80]. Since the context is different (TO filtering versus TO heterodyne beamforming, linear array versus phased array, affine model-based method versus

improve the lateral shear (and lateral strain) estimation. This is an avenue that may deserve to be explored.

In this study, we used the 2-D plane strain assumption for both LSME and APBE, and consequently the out-of-plane motion was not considered. This out-of-plane motion likely occurs if one considers non-homogenous human plaques and that motion may undermine the speckle or phase coherence in this direction. Fortunately, the models we presented here can be extended to 3-D. Combined with a 3-D data acquisition transducer, this would allow the LSME and APBE to estimate the full 3-D strain tensor while alleviating this assumption. In this study, the out-of-plane motion was also neglected for the incompressibility constraint. The isovolumic assumption used in Section 2.2.4 was indeed based on 3-D deformations. This is another aspect that would need to be further investigated.

6. Conclusion

In this paper, two affine model-based estimators were studied under the framework of high frame rate imaging. A time-ensemble approach and an incompressibility constraint were introduced to improve the performance of the affine phase-based estimator (APBE) for principal strain measurements. We also evaluated the performance of the APBE against the Lagrangian speckle model estimator (LSME), which also considered the time-ensemble strategy, with or without the incompressibility constraint. For all tested conditions, using the incompressibility constraint outperformed other implementations. In the simulation study, the LSME gave less principal strain estimation errors than the developed APBE. For the *in vitro* study, LSME elastograms provided higher SNRs for a homogeneous phantom, and higher SNRs and CNRs than the developed APBE over a wide range of strain values. In general, the LSME without TO filtering provided better results. Nonetheless, comparable or better principal strain estimates could be obtained with the LSME and TO filtering in the case of complex and heterogeneous tissue structures (with the incompressibility assumption).

Acknowledgments

This work was supported by the Collaborative Health Research Program of the Natural Sciences and Engineering Research Council of Canada (CHRP-462240-2014) and the Canadian Institutes of Health Research (CPG-134748).

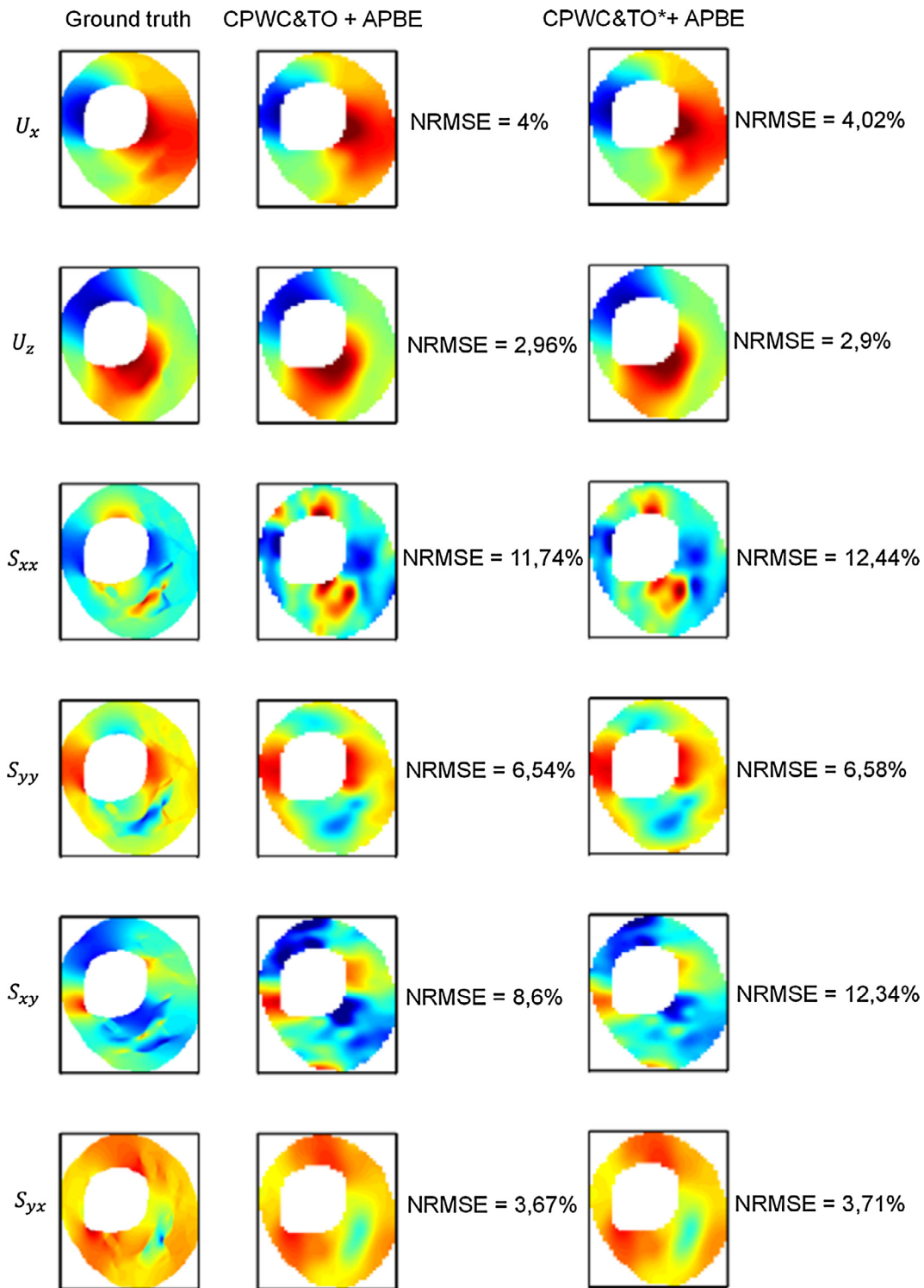


Fig. A1. Ground truth of motion components from finite-element model (first column) and motion components estimated with the APBE on CPWC&TO beamformed data (second column) and CPWC&TO with heterodyne demodulation data (third column). Note that the incompressibility constraint was not used to better appreciate the influence of the heterodyne demodulation on each motion component. The strain components were also not combined to obtain principal strains for this example.

correlation-based method, etc.), the comparison might be misleading because different types of images and estimators were considered. Firstly, in [80], the conclusion was based on the Cramer-Rao Lower Bound (CRLB) formulation to predict the minimum attainable standard deviation of the jitter of displacement estimates of an unbiased motion estimator. Three parameters determine the jitter in the CRLB equation, the decorrelation, frequency content and SNR of beamformed signals. Our affine-based estimators (APBE and LSME) are not correlation-based methods so decorrelation was not computed. Moreover, the LSME is a biased estimator which requires good image gradient correlation instead of image intensity correlation. Secondly, in the current study, we derived strains using an affine model and a minimization procedure. It is a nonlinear process that is more complex than deriving displacements. The conclusions on displacement estimations may thus not be applicable. According to results reported in this section, we judged inappropriate to also test the LSME estimator with heterodyne demodulated images.

References

- [1] R. Nayak, H. Steven, J. Ohayon, N. Carson, V. Dogra, G. Schifitto, M.M. Doyley, Principal strain vascular elastography: simulation and preliminary clinical evaluation, *Ultrasound Med. Biol.* 43 (2016) 1–18.
- [2] M.M. Doyley, J.C. Bamber, F. Fuechsel, N.L. Bush, A freehand elastographic imaging approach for clinical breast imaging: system development and performance evaluation, *Ultrasound Med. Biol.* 27 (2001) 1347–1357.
- [3] J. Luo, E.E. Konofagou, A fast normalized cross-correlation calculation method for motion estimation, *IEEE Trans. Ultrason. Ferroelectr. Freq. Control* 57 (2010) 1347–1357.
- [4] R.G.P. Lopata, M.M. Nillesen, H.H.G. Hansen, I.H. Gerrits, J.M. Thijssen, C.L. de Korte, Performance evaluation of methods for two-dimensional displacement and strain estimation using ultrasound radio frequency data, *Ultrasound Med. Biol.* 35 (2009) 796–812.
- [5] S. Korukonda, M.M. Doyley, Visualizing the radial and circumferential strain distribution within vessel phantoms using synthetic-aperture ultrasound elastography, *IEEE Trans. Ultrason. Ferroelectr. Freq. Control* 59 (2012) 1639–1653.
- [6] M. Larsson, B. Heyde, F. Kremer, L.-Å. Brodin, J. D'hooge, Ultrasound speckle tracking for radial, longitudinal and circumferential strain estimation of the carotid artery – an in vitro validation via sonomicrometry using clinical and high-frequency ultrasound, *Ultrasonics* 56 (2015) 399–408.
- [7] M.A. Lubinski, S.Y. Emelianov, M. O'Donnell, Speckle tracking methods for ultrasonic elasticity imaging using short-time correlation, *IEEE Trans. Ultrason. Ferroelectr. Freq. Control* 46 (1999) 82–96.
- [8] H.H.G. Hansen, R.G.P. Lopata, T. Idzenga, C.L. de Korte, Full 2D displacement vector and strain tensor estimation for superficial tissue using beam-steered ultrasound imaging, *Phys. Med. Biol.* 55 (2010) 3201–3218.
- [9] S. Golemati, A. Sassano, M.J. Lever, A.A. Bharath, S. Dhanjil, A.N. Nicolaides, Carotid artery wall motion estimated from b-mode ultrasound using region tracking and block matching, *Ultrasound Med. Biol.* 29 (2003) 387–399.
- [10] H. Li, Y. Guo, W.-N. Lee, Systematic performance evaluation of a cross-correlation-based ultrasound strain imaging method, *Ultrasound Med. Biol.* 42 (2016) 2436–2456.
- [11] K. Kaluzynski, X. Chen, S.Y. Emelianov, A.R. Skovoroda, M. O'Donnell, Strain rate imaging using two-dimensional speckle tracking, *IEEE Trans. Ultrason. Ferroelectr. Freq. Control* 48 (2001) 1111–1123.
- [12] X. Chen, M. Zohdy, S.Y. Emelianov, M. O'Donnell, Lateral speckle tracking using synthetic lateral phase, *IEEE Trans. Ultrason. Ferroelectr. Freq. Control* 51 (2004) 540–550.
- [13] E.S. Ebbini, Phase-coupled two-dimensional speckle tracking algorithm, *IEEE Trans. Ultrason. Ferroelectr. Freq. Control* 53 (2006) 972–990.
- [14] E. Brusseau, J. Kybic, J.F. D eprez, O. Basset, 2-D locally regularized tissue strain estimation from radio-frequency ultrasound images: Theoretical developments and results on experimental data, *IEEE Trans. Med. Imag.* 27 (2008) 145–160.
- [15] H. Rivaz, E. Boctor, P. Foroughi, R. Zellars, G. Fichtinger, G. Hager, Ultrasound elastography: a dynamic programming approach, *IEEE Trans. Med. Imag.* 27 (2008) 1373–1377.
- [16] V. Behar, D. Adam, P. Lysyansky, Z. Friedman, Improving motion estimation by accounting for local image distortion, *Ultrasonics* 43 (2004) 57–65.
- [17] S.K. Alam, J. Ophir, Reduction of signal decorrelation from mechanical compression of tissues by temporal stretching: applications to elastography, *Ultrasound Med. Biol.* 23 (1997) 95–105.
- [18] H. Chen, H. Shi, T. Varghese, Improvement of elastographic displacement estimation using a two-step cross-correlation method, *Ultrasound Med. Biol.* 33 (2008) 48–56.
- [19] H. Shi, T. Varghese, Two-dimensional multi-level strain estimation for discontinuous tissue, *Phys. Med. Biol.* 52 (2007) 389–401.
- [20] S.K. Alam, J. Ophir, E.E. Konofagou, An adaptive strain estimator for elastography, *IEEE Trans. Ultrason. Ferroelectr. Freq. Control* 45 (1998) 461–472.
- [21] R.G.P. Lopata, H. Hansen, M. Nillesen, J. Thijssen, L. Kapusta, C.L. de Korte, Methodical study on the estimation of strain in shearing and rotating structures using radio frequency ultrasound based on 1-D and 2-D strain estimation techniques, *IEEE Trans. Ultrason. Ferroelectr. Freq. Control* 57 (2010) 855–865.
- [22] R.L. Maurice, J. Ohayon, Y. Fretigny, M. Bertrand, G. Soulez, G. Cloutier, Noninvasive vascular elastography: theoretical framework, *IEEE Trans. Med. Imag.* 23 (2004) 164–180.
- [23] K. Liu, P. Zhang, J. Shao, X. Zhu, Y. Zhang, J. Bai, A 2D strain estimator with numerical optimization method for soft-tissue elastography, *Ultrasonics* 49 (2009) 723–732.
- [24] E. Mercure, G. Cloutier, C. Schmitt, R.L. Maurice, Performance evaluation of different implementations of the Lagrangian speckle model estimator for non-invasive vascular ultrasound elastography, *Med. Phys.* 35 (2008) 3116–3126.
- [25] X. Pan, J. Gao, S. Tao, K. Liu, J. Bai, J. Luo, A two-step optical flow method for strain estimation in elastography: simulation and phantom study, *Ultrasonics* 54 (2014) 990–996.
- [26] M. Alessandrini, A. Basarab, L. Bussel, X. Guo, A. Serusclat, D. Friboulet, D. Kouam e, O. Bernard, H. Liebgott, A new technique for the estimation of cardiac motion in echocardiography based on transverse oscillations: a preliminary evaluation in silico and a feasibility demonstration in vivo, *IEEE Trans. Med. Imag.* 33 (2014) 1148–1162.
- [27] J. Por e, D. Garc a, B. Chayer, J. Ohayon, G. Cloutier, Non-invasive vascular elastography with plane strain incompressibility assumption using ultrafast coherent compound plane wave imaging, *IEEE Trans. Med. Imag.* 34 (2015) 2618–2631.
- [28] A. Basarab, P. Gueth, H. Liebgott, P. Delachartre, Phase-based block matching applied to motion estimation with unconventional beamforming strategies, *IEEE Trans. Ultrason. Ferroelectr. Freq. Control* 56 (2009) 945–957.
- [29] A. Basarab, H. Liebgott, P. Delachartre, Analytic estimation of subsample spatial shift using the phases of multidimensional analytic signals, *IEEE Trans. Image Process* 18 (2009) 440–447.
- [30] F. Varray, H. Liebgott, Multi-resolution transverse oscillation in ultrasound imaging for motion estimation, *IEEE Trans. Ultrason. Ferroelectr. Freq. Control* 60 (2013) 1333–1342.
- [31] M.A. Lubinski, S.Y. Emelianov, K.R. Raghavan, A.E. Yagle, A.R. Skovoroda, M. O'Donnell, Lateral displacement estimation using tissue incompressibility, *IEEE Trans. Ultrason. Ferroelectr. Freq. Control* 43 (1996) 247–256.
- [32] E. Konofagou, J. Ophir, A new elastographic method for estimation and imaging of lateral displacements, lateral strains, corrected axial strains and Poisson's ratios in tissues, *Ultrasound Med. Biol.* 24 (1998) 1183–1199.
- [33] U. Techavipoo, Q. Chen, T. Varghese, J.A. Zagzebski, Estimation of displacement vectors and strain tensors in elastography using angular insonifications, *IEEE Trans Med Imag.* 23 (2004) 1479–1489.
- [34] R. Min, Q. Chen, H. Shi, Spatial-angular compounding for elastography using beam steering on linear array transducers, *Med. Phys.* 33 (2007) 618–626.
- [35] H.H.G. Hansen, R.G.P. Lopata, C.L. De Korte, Noninvasive carotid strain imaging using angular compounding at large beam steered angles: Validation in vessel phantoms, *IEEE Trans. Med. Imag.* 28 (2009) 872–880.
- [36] H.H.G. Hansen, R.G.P. Lopata, T. Idzenga, C.L. de Korte, An angular compounding technique using displacement projection for noninvasive ultrasound strain imaging of vessel cross-sections, *Ultrasound Med. Biol.* 36 (2010) 1947–1956.
- [37] S. Korukonda, M.M. Doyley, Estimating axial and lateral strain using a synthetic aperture elastographic imaging system, *Ultrasound Med. Biol.* 37 (2011) 1893–1908.
- [38] S. Korukonda, R. Nayak, N. Carson, G. Schifitto, V. Dogra, M.M. Doyley, Noninvasive vascular elastography using plane-wave and sparse-array imaging, *IEEE Trans. Ultrason. Ferroelectr. Freq. Control* 60 (2013) 332–342.
- [39] H.H.G. Hansen, A.E.C.M. Saris, N.R. Vaka, M.M. Nillesen, C.L. de Korte, Ultrafast vascular strain compounding using plane wave transmission, *J. Biomech.* 47 (2014) 815–823.
- [40] J. Zhao, Y. Wang, X. Zeng, J. Yu, B.Y.S. Yiu, A.C.H. Yu, Plane wave compounding based on a joint transmitting-receiving adaptive beamformer, *IEEE Trans. Ultrason. Ferroelectr. Freq. Control* 62 (2015) 1440–1452.
- [41] G. Montaldo, M. Tanter, J. Bercoff, N. Benez, M. Fink, Coherent plane-wave compounding for very high frame rate ultrasonography and transient elastography, *IEEE Trans. Ultrason. Ferroelectr. Freq. Control* 56 (2009) 489–506.
- [42] M.E. Aderson, Multi-dimensional velocity estimation with ultrasound using spatial quadrature, *IEEE Trans. Ultrason. Ferroelectr. Freq. Control* 45 (1998) 852–861.
- [43] J.A. Jensen, P. Munk, A new method for estimation of velocity vectors, *IEEE Trans. Ultrason. Ferroelectr. Freq. Control* 45 (1998) 837–851.
- [44] J.A. Jensen, A new estimator for vector velocity estimation, *IEEE Trans. Ultrason. Ferroelectr. Freq. Control* 48 (2001) 886–894.
- [45] S. Salles, A.J.Y. Chee, D. Garcia, A.C.H. Yu, D. Vray, H. Liebgott, 2-D arterial wall motion imaging using ultrafast ultrasound and transverse oscillations, *IEEE Trans. Ultrason. Ferroelectr. Freq. Control* 62 (2015) 1047–1058.
- [46] S. Salles, D. Garcia, B. Bou-said, F. Savary, A. S erusclat, D. Vray, Plane Wave Transverse Oscillation (PWTO): an ultrafast transverse oscillation imaging mode performed in the Fourier domain for 2D motion estimation of the carotid artery, in: *IEEE Int. Symp. Biomed. Imaging*, 2014, pp. 1409–1412.
- [47] H. Liebgott, A. Basarab, P. Gueth, D. Friboulet, P. Delachartre, Transverse oscillations for tissue motion estimation, *Ultrasonics* 50 (2010) 548–555.
- [48] Index of/ius-special-issue-2014, *Creatis.insa-lyon.fr*, 2014. < <http://www.creatis.insa-lyon.fr/ius-special-issue-2014/> > .
- [49] D.R. Nolan, J.P. McGarry, On the compressibility of arterial tissue, *Ann. Biomed. Eng.* 44 (2016) 993–1007.
- [50] R.A. Baldeewing, J.A. Schaar, F. Mastik, C.W.J. Oomens, A.F.W. van der Steen, Assessment of vulnerable plaque composition by matching the deformation of a parametric plaque model to measured plaque deformation, *IEEE Trans. Med. Imag.* 24 (2005) 514–528.
- [51] P. Chaturvedi, M.F. Insana, 2-D companding for noise reduction in strain imaging, *IEEE Trans. Ultrason. Ferroelectr. Freq. Control* 45 (1998) 179–191.
- [52] T. Liang, L. Yung, W. Yu, On feature motion decorrelation in ultrasound speckle tracking, *IEEE Trans. Med. Imag.* 32 (2013) 435–448.
- [53] U. Techavipoo, Q. Chen, T. Varghese, J.A. Zagzebski, E.L. Madsen, Noise reduction using spatial-angular compounding for elastography, *IEEE Trans. Ultrason. Ferroelectr. Freq. Control* 51 (2004) 510–520.
- [54] S. Le Floch, J. Ohayon, P. Tracqui, G. Finet, A.M. Gharib, R.L. Maurice, G. Cloutier, R.I. Pettigrew, Vulnerable atherosclerotic plaque elasticity reconstruction based on a segmentation-driven optimization procedure using strain measurements: theoretical framework, *IEEE Trans. Med. Imag.* 28 (2009) 1126–1137.
- [55] T.E. Carew, R.N. Vaishnav, D.J. Patel, Compressibility of the arterial wall, *Circ. Res.* 23 (1968) 61–68.
- [56] X.J. Girerd, C. Acar, J.-J. Mourad, P. Boutouyrie, M.E. Safar, S. Laurent, Incompressibility of the human arterial wall: an in vitro ultrasound study, *J. Hypert.* 10 (1992) S111–S114.
- [57] A. Karimi, T. Sera, S. Kudo, Experimental verification of the healthy and atherosclerotic coronary arteries incompressibility via Digital Image Correlation, *Artery Res.* 16 (2016) 1–7.
- [58] J. Fromageau, J.L. Gennisson, C. Schmitt, R.L. Maurice, R. Mongrain, G. Cloutier, Estimation of polyvinyl alcohol cryogel mechanical properties with four ultrasound

- elastography methods and comparison with gold standard testings, *IEEE Trans. Ultrason. Ferroelectr. Freq. Control* 54 (2007) 498–508.
- [59] C.D. Meinhart, S.T. Wereley, J.G. Santiago, A PIV algorithm for estimating time-averaged velocity fields, *J. Fluids Eng.* 122 (2000) 285–289.
- [60] P.W. Holland, R.E. Welsch, Robust regression using iteratively reweighted least-squares, *Commun. Stat. Methods* 6 (1977) 813–827.
- [61] J. Porée, B. Chayer, G. Soulez, J. Ohayon, G. Cloutier, Noninvasive vascular modulography method for imaging the local elasticity of atherosclerotic plaques: simulation and in vitro vessel phantom study, *IEEE Trans. Ultrason. Ferroelectr. Freq. Control* 64 (2017) 1805–1817.
- [62] A.C. Akyildiz, L. Speelman, F.J.H. Gijzen, Mechanical properties of human atherosclerotic intima tissue, *J. Biomech.* 47 (2014) 773–783.
- [63] G.C. Cheng, H.M. Loree, R.D. Kamm, M.C. Fishbein, R.T. Lee, Distribution of circumferential stress in ruptured and stable atherosclerotic lesions. A structural analysis with histopathological correlation, *Circulation* 87 (1993) 1179–1187.
- [64] G. Finet, J. Ohayon, G. Rioufol, Biomechanical interaction between cap thickness, lipid core composition and blood pressure in vulnerable coronary plaque: impact on stability or instability, *Coron. Artery Dis.* 15 (2004) 13–20.
- [65] A. Bouvier, F. Deleaval, M.M. Doyley, S.K. Yazdani, G. Finet, S. Le Floch, G. Cloutier, R.I. Pettigrew, J. Ohayon, A direct vulnerable atherosclerotic plaque elasticity reconstruction method based on an original material-finite element formulation: theoretical framework, *Phys. Med. Biol.* 58 (2013) 8457–8476.
- [66] A. Tacheau, S. Le Floch, G. Finet, M.M. Doyley, R.I. Pettigrew, G. Cloutier, J. Ohayon, The imaging modulography technique revisited for high-definition intravascular ultrasound: theoretical framework, *Ultrasound Med. Biol.* 42 (2016) 727–741.
- [67] J.A. Jensen, Field: A program for simulating ultrasound systems, *Med. Biol. Eng. Comput.* 34 (1996) 351–353.
- [68] R.F. Wagner, S.W. Smith, J.M. Sandrik, H. Lopez, Statistics of speckle in ultrasound B-Scans, *IEEE Trans. Sonics Ultrason.* 30 (1983) 156–163.
- [69] G.T. Mase, G.E. Mase, *Continuum Mechanics for Engineers*, 1992.
- [70] B.M. Shapo, J.R. Crowe, A.R. Skovoroda, M.J. Eberle, N.A. Cohn, M. O'Donnell, Displacement and strain imaging of coronary arteries with intraluminal ultrasound, *IEEE Trans. Ultrason. Ferroelectr. Freq. Control* 43 (1996) 234–246.
- [71] S. Salles, H. Liebgott, D. Garcia, D. Vray, Full 3-D transverse oscillations: a method for tissue motion estimation, *IEEE Trans. Ultrason. Ferroelectr. Freq. Control* 62 (2015) 1473–1485.
- [72] T. Hastie, R. Tibshirani, J. Friedman, *The elements of statistical learning*, *Elements* 1 (2009) 337–387.
- [73] C. Ferm, D. Shulman, Y. Aloimonos, The statistics of optical flow, *Comput. Vis. Image Underst.* 82 (2001) 1–32.
- [74] B. Byram, S. Member, G.E. Trahey, M. Palmeri, Bayesian speckle tracking. Part II: biased ultrasound displacement estimation, *IEEE Trans. Ultrason. Ferroelectr. Freq. Control* 60 (2013) 144–157.
- [75] Z. Corbyn, Stroke: a growing global burden, *Nature* 510 (2014) 5–6.
- [76] J. Blacher, B. Pannier, A.P. Guerin, S.J. Marchais, M.E. Safar, G.M. London, Carotid arterial stiffness as a predictor of cardiovascular and all-cause mortality in end-stage renal disease, *Hypertension* 32 (1998) 570–574.
- [77] L. Cardoso, S. Weinbaum, Changing views of the biomechanics of vulnerable plaque rupture: a review, *Ann. Biomed. Eng.* 42 (2014) 415–431.
- [78] J. Capon, High-resolution frequency-wavenumber spectrum analysis, *Proc. IEEE* 57 (1969) 1408–1418.
- [79] N. Bottenus, G.E. Trahey, Evaluation of the transverse oscillation method using the Cramer-Rao Lower Bound, *IEEE Trans. Ultrason. Ferroelectr. Freq. Control* 62 (2015) 1–16.
- [80] B. Heyde, N. Bottenus, D. Jan, G.E. Trahey, Evaluation of the transverse oscillation technique for cardiac phased array imaging: a theoretical study, *IEEE Trans. Ultrason. Ferroelectr. Freq. Control* 64 (2017) 320–334.